Version of Record: https://www.sciencedirect.com/science/article/pii/S0021999118307125
Manuscript_4b4f578d1b2d792cac6bf6ac509f1e2a

Physics-Informed Neural Networks: A Deep Learning Framework for Solving Forward and Inverse Problems Involving Nonlinear Partial Differential Equations

M. Raissi[1], P. Perdikaris[2] and G.E. Karniadakis[1]

[1] *Division of Applied Mathematics, Brown University, Providence, RI, 02912, USA*
[2] *Department of Mechanical Engineering and Applied Mechanics, University of Pennsylvania, Philadelphia, PA, 19104, USA*

Abstract

We introduce *physics-informed neural networks* – neural networks that are trained to solve supervised learning tasks while respecting any given laws of physics described by general nonlinear partial differential equations. In this work, we present our developments in the context of solving two main classes of problems: data-driven solution and data-driven discovery of partial differential equations. Depending on the nature and arrangement of the available data, we devise two distinct types of algorithms, namely continuous time and discrete time models. The first type of models forms a new family of *data-efficient* spatio-temporal function approximators, while the latter type allows the use of arbitrarily accurate implicit Runge-Kutta time stepping schemes with unlimited number of stages. The effectiveness of the proposed framework is demonstrated through a collection of classical problems in fluids, quantum mechanics, reaction-diffusion systems, and the propagation of nonlinear shallow-water waves.

Keywords: Data-driven scientific computing, Machine learning, Predictive modeling, Runge-Kutta methods, Nonlinear dynamics

1. Introduction

With the explosive growth of available data and computing resources, recent advances in machine learning and data analytics have yielded trans-

formative results across diverse scientific disciplines, including image recognition [1], cognitive science [2], and genomics [3]. However, more often than not, in the course of analyzing complex physical, biological or engineering systems, the cost of data acquisition is prohibitive, and we are inevitably faced with the challenge of drawing conclusions and making decisions under partial information. In this *small data* regime, the vast majority of state-of-the-art machine learning techniques (e.g., deep/convolutional/recurrent neural networks) are lacking robustness and fail to provide any guarantees of convergence.

At first sight, the task of training a deep learning algorithm to accurately identify a nonlinear map from a few – potentially very high-dimensional – input and output data pairs seems at best naive. Coming to our rescue, for many cases pertaining to the modeling of physical and biological systems, there exists a vast amount of prior knowledge that is currently not being utilized in modern machine learning practice. Let it be the principled physical laws that govern the time-dependent dynamics of a system, or some empirically validated rules or other domain expertise, this prior information can act as a regularization agent that constrains the space of admissible solutions to a manageable size (e.g., in incompressible fluid dynamics problems by discarding any non realistic flow solutions that violate the conservation of mass principle). In return, encoding such structured information into a learning algorithm results in amplifying the information content of the data that the algorithm sees, enabling it to quickly steer itself towards the right solution and generalize well even when only a few training examples are available.

The first glimpses of promise for exploiting structured prior information to construct data-efficient and physics-informed learning machines have already been showcased in the recent studies of [4–6]. There, the authors employed Gaussian process regression [7] to devise functional representations that are tailored to a given linear operator, and were able to accurately infer solutions and provide uncertainty estimates for several prototype problems in mathematical physics. Extensions to nonlinear problems were proposed in subsequent studies by Raissi *et. al.* [8, 9] in the context of both inference and systems identification. Despite the flexibility and mathematical elegance of Gaussian processes in encoding prior information, the treatment of nonlinear problems introduces two important limitations. First, in [8, 9] the authors had to locally linearize any nonlinear terms in time, thus limiting the applica-

bility of the proposed methods to discrete-time domains and compromising the accuracy of their predictions in strongly nonlinear regimes. Secondly, the Bayesian nature of Gaussian process regression requires certain prior assumptions that may limit the representation capacity of the model and give rise to robustness/brittleness issues, especially for nonlinear problems [10].

2. Problem setup

In this work we take a different approach by employing deep neural networks and leverage their well known capability as universal function approximators [11]. In this setting, we can directly tackle nonlinear problems without the need for committing to any prior assumptions, linearization, or local time-stepping. We exploit recent developments in automatic differentiation [12] – one of the most useful but perhaps under-utilized techniques in scientific computing – to differentiate neural networks with respect to their input coordinates and model parameters to obtain *physics-informed neural networks*. Such neural networks are constrained to respect any symmetries, invariances, or conservation principles originating from the physical laws that govern the observed data, as modeled by general time-dependent and nonlinear partial differential equations. This simple yet powerful construction allows us to tackle a wide range of problems in computational science and introduces a potentially transformative technology leading to the development of new data-efficient and physics-informed learning machines, new classes of numerical solvers for partial differential equations, as well as new data-driven approaches for model inversion and systems identification.

The general aim of this work is to set the foundations for a new paradigm in modeling and computation that enriches deep learning with the longstanding developments in mathematical physics. To this end, our manuscript is divided into two parts that aim to present our developments in the context of two major classes of problems: data-driven solution and data-driven discovery of partial differential equations. All code and data-sets accompanying this manuscript are available on GitHub at `https://github.com/maziarraissi/PINNs`. Throughout this work we have been using relatively simple deep feed-forward neural networks architectures with hyperbolic tangent activation functions and no additional regularization (e.g., L1/L2 penalties, dropout, etc.). Each numerical example in the manuscript is accompanied with a detailed discussion about the neural network architecture we

employed as well as details about its training process (e.g. optimizer, learning rates, etc.). Finally, a comprehensive series of systematic studies that aims to demonstrate the performance of the proposed methods is provided in Appendix A and Appendix B.

In this work, we consider parametrized and nonlinear partial differential equations of the general form

$$u_t + \mathcal{N}[u; \lambda] = 0, \ x \in \Omega, \ t \in [0, T], \tag{1}$$

where $u(t, x)$ denotes the latent (hidden) solution, $\mathcal{N}[\cdot; \lambda]$ is a nonlinear operator parametrized by λ, and Ω is a subset of $\mathbb{R}^D$. This setup encapsulates a wide range of problems in mathematical physics including conservation laws, diffusion processes, advection-diffusion-reaction systems, and kinetic equations. As a motivating example, the one dimensional Burgers equation [13] corresponds to the case where $\mathcal{N}[u; \lambda] = \lambda_1 u u_x - \lambda_2 u_{xx}$ and $\lambda = (\lambda_1, \lambda_2)$. Here, the subscripts denote partial differentiation in either time or space. Given noisy measurements of the system, we are interested in the solution of two distinct problems. The first problem is that of inference, filtering and smoothing, or data-driven solutions of partial differential equations [4, 8] which states: *given fixed model parameters λ what can be said about the unknown hidden state $u(t, x)$ of the system?* The second problem is that of learning, system identification, or data-driven discovery of partial differential equations [5, 9, 14] stating: *what are the parameters λ that best describe the observed data?*

3. Data-driven solutions of partial differential equations

Let us start by concentrating on the problem of computing data-driven solutions to partial differential equations (i.e., the first problem outlined above) of the general form

$$u_t + \mathcal{N}[u] = 0, \ x \in \Omega, \ t \in [0, T], \tag{2}$$

where $u(t, x)$ denotes the latent (hidden) solution, $\mathcal{N}[\cdot]$ is a nonlinear differential operator, and Ω is a subset of $\mathbb{R}^D$. In sections 3.1 and 3.2, we put forth two distinct types of algorithms, namely continuous and discrete time models, and highlight their properties and performance through the lens of different benchmark problems. In the second part of our study (see section 4), we shift our attention to the problem of data-driven discovery of partial differential equations [5, 9, 14].

3.1. Continuous Time Models

We define $f(t,x)$ to be given by the left-hand-side of equation (2); i.e.,

$$f := u_t + \mathcal{N}[u], \tag{3}$$

and proceed by approximating $u(t,x)$ by a deep neural network. This assumption along with equation (3) result in a *physics-informed neural network* $f(t,x)$. This network can be derived by applying the chain rule for differentiating compositions of functions using automatic differentiation [12], and has the same parameters as the network representing $u(t,x)$, albeit with different activation functions due to the action of the differential operator $\mathcal{N}$. The shared parameters between the neural networks $u(t,x)$ and $f(t,x)$ can be learned by minimizing the mean squared error loss

$$MSE = MSE_u + MSE_f, \tag{4}$$

where

$$MSE_u = \frac{1}{N_u}\sum_{i=1}^{N_u} |u(t_u^i, x_u^i) - u^i|^2,$$

and

$$MSE_f = \frac{1}{N_f}\sum_{i=1}^{N_f} |f(t_f^i, x_f^i)|^2.$$

Here, $\{t_u^i, x_u^i, u^i\}_{i=1}^{N_u}$ denote the initial and boundary training data on $u(t,x)$ and $\{t_f^i, x_f^i\}_{i=1}^{N_f}$ specify the collocations points for $f(t,x)$. The loss MSE_u corresponds to the initial and boundary data while MSE_f enforces the structure imposed by equation (2) at a finite set of collocation points. Although similar ideas for constraining neural networks using physical laws have been explored in previous studies [15, 16], here we revisit them using modern computational tools, and apply them to more challenging dynamic problems described by time-dependent nonlinear partial differential equations.

Here, we should underline an important distinction between this line of work and existing approaches in the literature that elaborate on the use of machine learning in computational physics. The term *physics-informed machine learning* has been also recently used by Wang *et. al.* [17] in the context of turbulence modeling. Other examples of machine learning approaches for predictive modeling of physical systems include [18–29]. All these approaches

employ machine learning algorithms like support vector machines, random forests, Gaussian processes, and feed-forward/convolutional/recurrent neural networks merely as *black-box* tools. As described above, the proposed work aims to go one step further by revisiting the construction of "custom" activation and loss functions that are tailored to the underlying differential operator. This allows us to open the black-box by understanding and appreciating the key role played by automatic differentiation within the deep learning field. Automatic differentiation in general, and the back-propagation algorithm in particular, is currently the dominant approach for training deep models by taking their derivatives with respect to the parameters (e.g., weights and biases) of the models. Here, we use the exact same automatic differentiation techniques, employed by the deep learning community, to physics-inform neural networks by taking their derivatives with respect to their input coordinates (i.e., space and time) where the physics is described by partial differential equations. We have empirically observed that this structured approach introduces a regularization mechanism that allows us to use relatively simple feed-forward neural network architectures and train them with small amounts of data. The effectiveness of this simple idea may be related to the remarks put forth by Lin, Tegmark and Rolnick [30] and raises many interesting questions to be quantitatively addressed in future research. To this end, the proposed work draws inspiration from the early contributions of Psichogios and Ungar [16], Lagaris *et. al.* [15], as well as the contemporary works of Kondor [31, 32], Hirn [33], and Mallat [34].

In all cases pertaining to data-driven solution of partial differential equations, the total number of training data N_u is relatively small (a few hundred up to a few thousand points), and we chose to optimize all loss functions using L-BFGS, a quasi-Newton, full-batch gradient-based optimization algorithm [35]. For larger data-sets, such as the data-driven model discovery examples discussed in section 4, a more computationally efficient mini-batch setting can be readily employed using stochastic gradient descent and its modern variants [36, 37]. Despite the fact that there is no theoretical guarantee that this procedure converges to a global minimum, our empirical evidence indicates that, if the given partial differential equation is well-posed and its solution is unique, our method is capable of achieving good prediction accuracy given a sufficiently expressive neural network architecture and a sufficient number of collocation points N_f. This general observation deeply relates to the resulting optimization landscape induced by the mean square error loss of

equation 4, and defines an open question for research that is in sync with recent theoretical developments in deep learning [38, 39]. To this end, we will test the robustness of the proposed methodology using a series of systematic sensitivity studies that are provided in Appendix A and Appendix B.

3.1.1. Example (Shrödinger Equation)

This example aims to highlight the ability of our method to handle periodic boundary conditions, complex-valued solutions, as well as different types of nonlinearities in the governing partial differential equations. The one-dimensional nonlinear Schrödinger equation is a classical field equation that is used to study quantum mechanical systems, including nonlinear wave propagation in optical fibers and/or waveguides, Bose-Einstein condensates, and plasma waves. In optics, the nonlinear term arises from the intensity dependent index of refraction of a given material. Similarly, the nonlinear term for Bose-Einstein condensates is a result of the mean-field interactions of an interacting, N-body system. The nonlinear Schrödinger equation along with periodic boundary conditions is given by

$$\begin{aligned} &ih_t + 0.5h_{xx} + |h|^2 h = 0, \quad x \in [-5, 5], \quad t \in [0, \pi/2], \\ &h(0, x) = 2 \text{ sech}(x), \\ &h(t, -5) = h(t, 5), \\ &h_x(t, -5) = h_x(t, 5), \end{aligned} \tag{5}$$

where $h(t, x)$ is the complex-valued solution. Let us define $f(t, x)$ to be given by

$$f := ih_t + 0.5h_{xx} + |h|^2 h,$$

and proceed by placing a complex-valued neural network prior on $h(t, x)$. In fact, if u denotes the real part of h and v is the imaginary part, we are placing a multi-out neural network prior on $h(t, x) = \begin{bmatrix} u(t, x) & v(t, x) \end{bmatrix}$. This will result in the complex-valued (multi-output) *physic-informed neural network* $f(t, x)$. The shared parameters of the neural networks $h(t, x)$ and $f(t, x)$ can be learned by minimizing the mean squared error loss

$$MSE = MSE_0 + MSE_b + MSE_f, \tag{6}$$

where

$$MSE_0 = \frac{1}{N_0} \sum_{i=1}^{N_0} |h(0, x_0^i) - h_0^i|^2,$$

$$MSE_b = \frac{1}{N_b}\sum_{i=1}^{N_b}\left(|h^i(t_b^i,-5)-h^i(t_b^i,5)|^2+|h_x^i(t_b^i,-5)-h_x^i(t_b^i,5)|^2\right),$$

and

$$MSE_f = \frac{1}{N_f}\sum_{i=1}^{N_f}|f(t_f^i,x_f^i)|^2.$$

Here, $\{x_0^i,h_0^i\}_{i=1}^{N_0}$ denotes the initial data, $\{t_b^i\}_{i=1}^{N_b}$ corresponds to the collocation points on the boundary, and $\{t_f^i,x_f^i\}_{i=1}^{N_f}$ represents the collocation points on $f(t,x)$. Consequently, MSE_0 corresponds to the loss on the initial data, MSE_b enforces the periodic boundary conditions, and MSE_f penalizes the Schrödinger equation not being satisfied on the collocation points.

In order to assess the accuracy of our method, we have simulated equation (5) using conventional spectral methods to create a high-resolution data set. Specifically, starting from an initial state $h(0,x) = 2\,\mathrm{sech}(x)$ and assuming periodic boundary conditions $h(t,-5) = h(t,5)$ and $h_x(t,-5) = h_x(t,5)$, we have integrated equation (5) up to a final time $t = \pi/2$ using the Chebfun package [40] with a spectral Fourier discretization with 256 modes and a fourth-order explicit Runge-Kutta temporal integrator with time-step $\Delta t = \pi/2\cdot 10^{-6}$. Under our data-driven setting, all we observe are measurements $\{x_0^i,h_0^i\}_{i=1}^{N_0}$ of the latent function $h(t,x)$ at time $t=0$. In particular, the training set consists of a total of $N_0 = 50$ data points on $h(0,x)$ randomly parsed from the full high-resolution data-set, as well as $N_b = 50$ randomly sampled collocation points $\{t_b^i\}_{i=1}^{N_b}$ for enforcing the periodic boundaries. Moreover, we have assumed $N_f = 20,000$ randomly sampled collocation points used to enforce equation (5) inside the solution domain. All randomly sampled point locations were generated using a space filling Latin Hypercube Sampling strategy [41].

Here our goal is to infer the entire spatio-temporal solution $h(t,x)$ of the Schrödinger equation (5). We chose to jointly represent the latent function $h(t,x) = [u(t,x)\ v(t,x)]$ using a 5-layer deep neural network with 100 neurons per layer and a hyperbolic tangent activation function. In general, the neural network should be given sufficient approximation capacity in order to accommodate the anticipated complexity of $u(t,x)$. Although more systematic procedures such as Bayesian optimization [42] can be employed in order

to fine-tune the design of the neural network, in the absence of theoretical error/convergence estimates, the interplay between the neural architecture/-training procedure and the complexity of the underlying differential equation is still poorly understood. One viable path towards assessing the accuracy of the predicted solution could come by adopting a Bayesian approach and monitoring the variance of the predictive posterior distribution, but this goes beyond the scope of the present work and will be investigated in future studies.

In this example, our setup aims to highlight the robustness of the proposed method with respect to the well known issue of over-fitting. Specifically, the term in MSE_f in equation (6) acts as a regularization mechanism that penalizes solutions that do not satisfy equation (5). Therefore, a key property of *physics-informed neural networks* is that they can be effectively trained using small data sets; a setting often encountered in the study of physical systems for which the cost of data acquisition may be prohibitive. Figure 1 summarizes the results of our experiment. Specifically, the top panel of figure 1 shows the magnitude of the predicted spatio-temporal solution $|h(t,x)| = \sqrt{u^2(t,x) + v^2(t,x)}$, along with the locations of the initial and boundary training data. The resulting prediction error is validated against the test data for this problem, and is measured at $1.97 \cdot 10^{-3}$ in the relative $\mathbb{L}_2$-norm. A more detailed assessment of the predicted solution is presented in the bottom panel of Figure 1. In particular, we present a comparison between the exact and the predicted solutions at different time instants $t = 0.59, 0.79, 0.98$. Using only a handful of initial data, the *physics-informed neural network* can accurately capture the intricate nonlinear behavior of the Schrödinger equation.

One potential limitation of the continuous time neural network models considered so far stems from the need to use a large number of collocation points N_f in order to enforce physics-informed constraints in the entire spatio-temporal domain. Although this poses no significant issues for problems in one or two spatial dimensions, it may introduce a severe bottleneck in higher dimensional problems, as the total number of collocation points needed to globally enforce a physics-informed constrain (i.e., in our case a partial differential equation) will increase exponentially. Although this limitation could be addressed to some extend using sparse grid or quasi Monte-Carlo sampling schemes [43, 44], in the next section, we put forth a different approach that circumvents the need for collocation points by in-

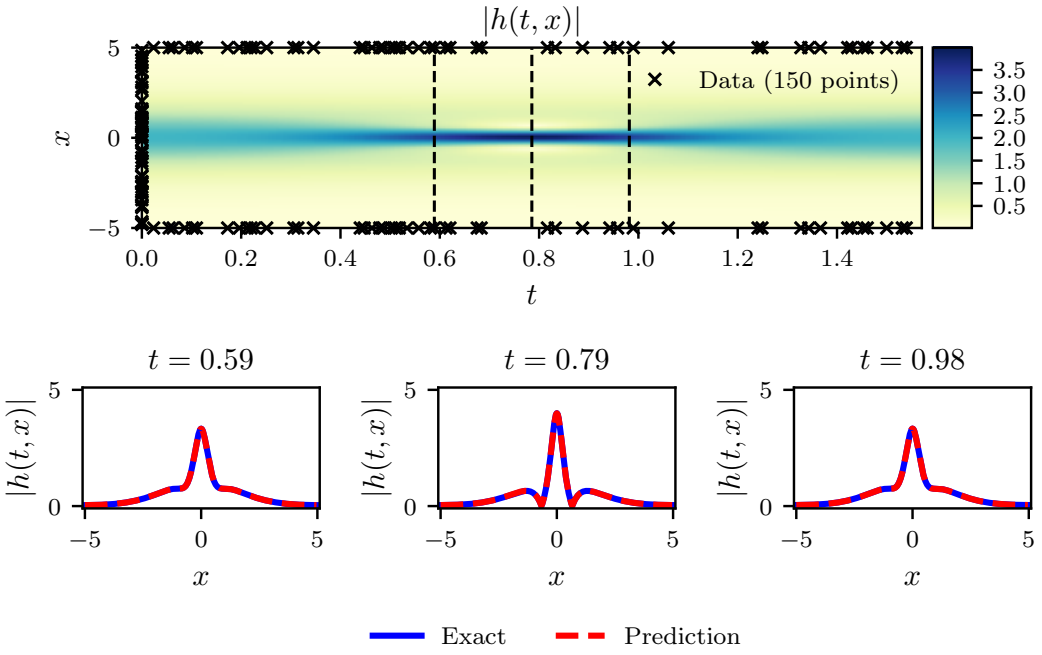

Figure 1: *Shrödinger equation: Top:* Predicted solution $|h(t,x)|$ along with the initial and boundary training data. In addition we are using 20,000 collocation points generated using a Latin Hypercube Sampling strategy. *Bottom:* Comparison of the predicted and exact solutions corresponding to the three temporal snapshots depicted by the dashed vertical lines in the top panel. The relative $\mathbb{L}_2$ error for this case is $1.97 \cdot 10^{-3}$.

troducing a more structured neural network representation leveraging the classical Runge-Kutta time-stepping schemes [45].

3.2. Discrete Time Models

Let us apply the general form of Runge-Kutta methods with q stages [45] to equation (2) and obtain

$$\begin{aligned} u^{n+c_i} &= u^n - \Delta t \textstyle\sum_{j=1}^{q} a_{ij} \mathcal{N}[u^{n+c_j}], \quad i = 1, \ldots, q, \\ u^{n+1} &= u^n - \Delta t \textstyle\sum_{j=1}^{q} b_j \mathcal{N}[u^{n+c_j}]. \end{aligned} \tag{7}$$

Here, $u^{n+c_j}(x) = u(t^n + c_j \Delta t, x)$ for $j = 1, \ldots, q$. This general form encapsulates both implicit and explicit time-stepping schemes, depending on the choice of the parameters $\{a_{ij}, b_j, c_j\}$. Equations (7) can be equivalently

expressed as

$$\begin{aligned} u^n &= u_i^n, \quad i = 1, \dots, q, \\ u^n &= u_{q+1}^n, \end{aligned} \tag{8}$$

where

$$\begin{aligned} u_i^n &:= u^{n+c_i} + \Delta t \sum_{j=1}^{q} a_{ij} \mathcal{N}[u^{n+c_j}], \quad i = 1, \dots, q, \\ u_{q+1}^n &:= u^{n+1} + \Delta t \sum_{j=1}^{q} b_j \mathcal{N}[u^{n+c_j}]. \end{aligned} \tag{9}$$

We proceed by placing a multi-output neural network prior on

$$\left[u^{n+c_1}(x), \dots, u^{n+c_q}(x), u^{n+1}(x)\right]. \tag{10}$$

This prior assumption along with equations (9) result in a *physics-informed neural network* that takes x as an input and outputs

$$\left[u_1^n(x), \dots, u_q^n(x), u_{q+1}^n(x)\right]. \tag{11}$$

3.2.1. Example (Allen-Cahn Equation)

This example aims to highlight the ability of the proposed discrete time models to handle different types of nonlinearity in the governing partial differential equation. To this end, let us consider the Allen-Cahn equation along with periodic boundary conditions

$$\begin{aligned} &u_t - 0.0001 u_{xx} + 5u^3 - 5u = 0, \quad x \in [-1, 1], \quad t \in [0, 1], \\ &u(0, x) = x^2 \cos(\pi x), \\ &u(t, -1) = u(t, 1), \\ &u_x(t, -1) = u_x(t, 1). \end{aligned} \tag{12}$$

The Allen-Cahn equation is a well-known equation from the area of reaction-diffusion systems. It describes the process of phase separation in multi-component alloy systems, including order-disorder transitions. For the Allen-Cahn equation, the nonlinear operator in equation (9) is given by

$$\mathcal{N}[u^{n+c_j}] = -0.0001 u_{xx}^{n+c_j} + 5\left(u^{n+c_j}\right)^3 - 5u^{n+c_j},$$

and the shared parameters of the neural networks (10) and (11) can be learned by minimizing the sum of squared errors

$$SSE = SSE_n + SSE_b, \tag{13}$$

where

$$SSE_n = \sum_{j=1}^{q+1} \sum_{i=1}^{N_n} |u_j^n(x^{n,i}) - u^{n,i}|^2,$$

and

$$\begin{aligned} SSE_b &= \sum_{i=1}^{q} |u^{n+c_i}(-1) - u^{n+c_i}(1)|^2 + |u^{n+1}(-1) - u^{n+1}(1)|^2 \\ &+ \sum_{i=1}^{q} |u_x^{n+c_i}(-1) - u_x^{n+c_i}(1)|^2 + |u_x^{n+1}(-1) - u_x^{n+1}(1)|^2. \end{aligned}$$

Here, $\{x^{n,i}, u^{n,i}\}_{i=1}^{N_n}$ corresponds to the data at time-step t^n. In classical numerical analysis, these time-steps are usually confined to be small due to stability constraints for explicit schemes or computational complexity constrains for implicit formulations [45]. These constraints become more severe as the total number of Runge-Kutta stages q is increased, and, for most problems of practical interest, one needs to take thousands to millions of such steps until the solution is resolved up to a desired final time. In sharp contrast to classical methods, here we can employ implicit Runge-Kutta schemes with an arbitrarily large number of stages at effectively very little extra cost.[1] This enables us to take very large time steps while retaining stability and high predictive accuracy, therefore allowing us to resolve the entire spatio-temporal solution in a single step.

In this example, we have generated a training and test data-set set by simulating the Allen-Cahn equation (12) using conventional spectral methods. Specifically, starting from an initial condition $u(0, x) = x^2 \cos(\pi x)$ and assuming periodic boundary conditions $u(t, -1) = u(t, 1)$ and $u_x(t, -1) = u_x(t, 1)$, we have integrated equation (12) up to a final time $t = 1.0$ using the Chebfun package [40] with a spectral Fourier discretization with 512 modes and a fourth-order explicit Runge-Kutta temporal integrator with time-step $\Delta t = 10^{-5}$.

Our training data-set consists of $N_n = 200$ initial data points that are randomly sub-sampled from the exact solution at time $t = 0.1$, and our goal

[1] To be precise, it is only the number of parameters in the last layer of the neural network that increases linearly with the total number of stages.

is to predict the solution at time $t = 0.9$ using a single time-step with size $\Delta t = 0.8$. To this end, we employ a discrete time *physics-informed neural network* with 4 hidden layers and 200 neurons per layer, while the output layer predicts 101 quantities of interest corresponding to the $q = 100$ Runge-Kutta stages $u^{n+c_i}(x)$, $i = 1, \ldots, q$, and the solution at final time $u^{n+1}(x)$. The theoretical error estimates for this scheme predict a temporal error accumulation of $\mathcal{O}(\Delta t^{2q})$ [45], which in our case translates into an error way below machine precision, i.e., $\Delta t^{2q} = 0.8^{200} \approx 10^{-20}$. To our knowledge, this is the first time that an implicit Runge-Kutta scheme of that high-order has ever been used. Remarkably, starting from smooth initial data at $t = 0.1$ we can predict the nearly discontinuous solution at $t = 0.9$ in a single time-step with a relative $\mathbb{L}_2$ error of $6.99 \cdot 10^{-3}$, as illustrated in Figure 2. This error is entirely attributed to the neural network's capacity to approximate $u(t, x)$, as well as to the degree that the sum of squared errors loss allows interpolation of the training data.

The key parameters controlling the performance of our discrete time algorithm are the total number of Runge-Kutta stages q and the time-step size Δt. As we demonstrate in the systematic studies provided in Appendix A and Appendix B, low-order methods, such as the case $q = 1$ corresponding to the classical trapezoidal rule, and the case $q = 2$ corresponding to the 4^{th}-order Gauss-Legendre method, cannot retain their predictive accuracy for large time-steps, thus mandating a solution strategy with multiple time-steps of small size. On the other hand, the ability to push the number of Runge-Kutta stages to 32 and even higher allows us to take very large time steps, and effectively resolve the solution in a single step without sacrificing the accuracy of our predictions. Moreover, numerical stability is not sacrificed either as implicit Gauss-Legendre is the only family of time-stepping schemes that remain A-stable regardless of their order, thus making them ideal for stiff problems [45]. These properties are unprecedented for an algorithm of such implementation simplicity, and illustrate one of the key highlights of our discrete time approach.

4. Data-driven discovery of partial differential equations

In the current part of our study, we shift our attention to the problem of data-driven discovery of partial differential equations [5, 9, 14]. In sections 4.1 and 4.2, we put forth two distinct types of algorithms, namely continuous

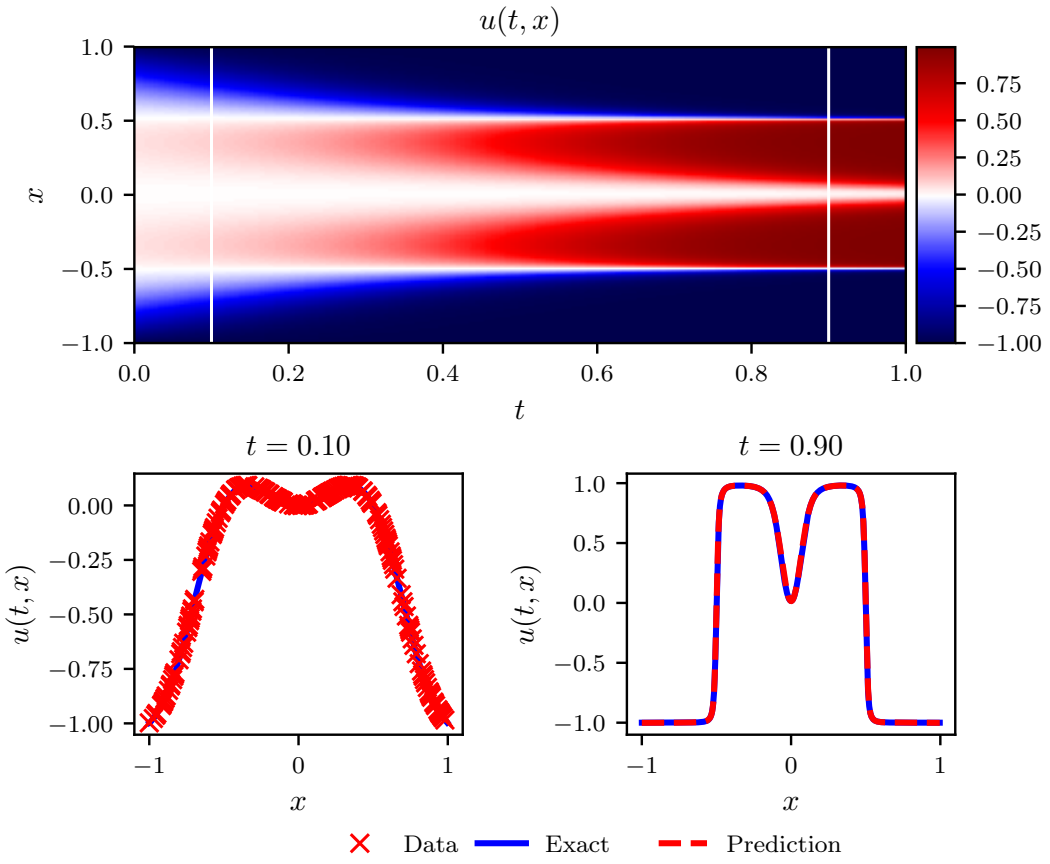

Figure 2: *Allen-Cahn equation: Top:* Solution $u(t,x)$ along with the location of the initial training snapshot at $t = 0.1$ and the final prediction snapshot at $t = 0.9$. *Bottom:* Initial training data and final prediction at the snapshots depicted by the white vertical lines in the top panel. The relative $\mathbb{L}_2$ error for this case is $6.99 \cdot 10^{-3}$.

and discrete time models, and highlight their properties and performance through the lens of various canonical problems.

4.1. Continuous Time Models

Let us recall equation (1) and similar to section 3.1 define $f(t,x)$ to be given by the left-hand-side of equation (1); i.e.,

$$f := u_t + \mathcal{N}[u;\lambda]. \tag{14}$$

We proceed by approximating $u(t,x)$ by a deep neural network. This assumption along with equation (14) result in a *physics-informed neural net-*

work $f(t, x)$. This network can be derived by applying the chain rule for differentiating compositions of functions using automatic differentiation [12]. It is worth highlighting that the parameters of the differential operator λ turn into parameters of the *physics-informed neural network* $f(t, x)$.

4.1.1. Example (Navier-Stokes Equation)

Our next example involves a realistic scenario of incompressible fluid flow described by the ubiquitous Navier-Stokes equations. Navier-Stokes equations describe the physics of many phenomena of scientific and engineering interest. They may be used to model the weather, ocean currents, water flow in a pipe and air flow around a wing. The Navier-Stokes equations in their full and simplified forms help with the design of aircrafts and cars, the study of blood flow, the design of power stations, the analysis of the dispersion of pollutants, and many other applications. Let us consider the Navier-Stokes equations in two dimensions[2] (2D) given explicitly by

$$\begin{aligned} u_t + \lambda_1(uu_x + vu_y) &= -p_x + \lambda_2(u_{xx} + u_{yy}), \\ v_t + \lambda_1(uv_x + vv_y) &= -p_y + \lambda_2(v_{xx} + v_{yy}), \end{aligned} \tag{15}$$

where $u(t, x, y)$ denotes the x-component of the velocity field, $v(t, x, y)$ the y-component, and $p(t, x, y)$ the pressure. Here, $\lambda = (\lambda_1, \lambda_2)$ are the unknown parameters. Solutions to the Navier-Stokes equations are searched in the set of divergence-free functions; i.e.,

$$u_x + v_y = 0. \tag{16}$$

This extra equation is the continuity equation for incompressible fluids that describes the conservation of mass of the fluid. We make the assumption that

$$u = \psi_y, \quad v = -\psi_x, \tag{17}$$

for some latent function $\psi(t, x, y)$.[3] Under this assumption, the continuity equation (16) will be automatically satisfied. Given noisy measurements

$$\{t^i, x^i, y^i, u^i, v^i\}_{i=1}^N$$

[2]It is straightforward to generalize the proposed framework to the Navier-Stokes equations in three dimensions (3D).

[3]This construction can be generalized to three dimensional problems by employing the notion of vector potentials.

of the velocity field, we are interested in learning the parameters λ as well as the pressure $p(t, x, y)$. We define $f(t, x, y)$ and $g(t, x, y)$ to be given by

$$\begin{aligned} f &:= u_t + \lambda_1(uu_x + vu_y) + p_x - \lambda_2(u_{xx} + u_{yy}), \\ g &:= v_t + \lambda_1(uv_x + vv_y) + p_y - \lambda_2(v_{xx} + v_{yy}), \end{aligned} \tag{18}$$

and proceed by jointly approximating $\begin{bmatrix}\psi(t,x,y) & p(t,x,y)\end{bmatrix}$ using a single neural network with two outputs. This prior assumption along with equations (17) and (18) results into a *physics-informed neural network* $\begin{bmatrix}f(t,x,y) & g(t,x,y)\end{bmatrix}$. The parameters λ of the Navier-Stokes operator as well as the parameters of the neural networks $\begin{bmatrix}\psi(t,x,y) & p(t,x,y)\end{bmatrix}$ and $\begin{bmatrix}f(t,x,y) & g(t,x,y)\end{bmatrix}$ can be trained by minimizing the mean squared error loss

$$\begin{aligned} MSE &:= \frac{1}{N}\sum_{i=1}^{N}\left(|u(t^i, x^i, y^i) - u^i|^2 + |v(t^i, x^i, y^i) - v^i|^2\right) \\ &+ \frac{1}{N}\sum_{i=1}^{N}\left(|f(t^i, x^i, y^i)|^2 + |g(t^i, x^i, y^i)|^2\right). \end{aligned} \tag{19}$$

Here we consider the prototype problem of incompressible flow past a circular cylinder; a problem known to exhibit rich dynamic behavior and transitions for different regimes of the Reynolds number $Re = u_\infty D/\nu$. Assuming a non-dimensional free stream velocity $u_\infty = 1$, cylinder diameter $D = 1$, and kinematic viscosity $\nu = 0.01$, the system exhibits a periodic steady state behavior characterized by a asymmetrical vortex shedding pattern in the cylinder wake, known as the Kármán vortex street [46].

To generate a high-resolution data set for this problem we have employed the spectral/*hp*-element solver NekTar [47]. Specifically, the solution domain is discretized in space by a tessellation consisting of 412 triangular elements, and within each element the solution is approximated as a linear combination of a tenth-order hierarchical, semi-orthogonal Jacobi polynomial expansion [47]. We have assumed a uniform free stream velocity profile imposed at the left boundary, a zero pressure outflow condition imposed at the right boundary located 25 diameters downstream of the cylinder, and periodicity for the top and bottom boundaries of the $[-15, 25] \times [-8, 8]$ domain. We integrate equation (15) using a third-order stiffly stable scheme [47] until the system reaches a periodic steady state, as depicted in figure 3(a). In what follows, a small portion of the resulting data-set corresponding to this steady state

solution will be used for model training, while the remaining data will be used to validate our predictions. For simplicity, we have chosen to confine our sampling in a rectangular region downstream of cylinder as shown in figure 3(a).

Given scattered and potentially noisy data on the stream-wise $u(t, x, y)$ and transverse $v(t, x, y)$ velocity components, our goal is to identify the unknown parameters λ_1 and λ_2, as well as to obtain a qualitatively accurate reconstruction of the entire pressure field $p(t, x, y)$ in the cylinder wake, which by definition can only be identified up to a constant. To this end, we have created a training data-set by randomly sub-sampling the full high-resolution data-set. To highlight the ability of our method to learn from scattered and scarce training data, we have chosen $N = 5,000$, corresponding to a mere 1% of the total available data as illustrated in figure 3(b). Also plotted are representative snapshots of the predicted velocity components $u(t, x, y)$ and $v(t, x, y)$ after the model was trained. The neural network architecture used here consists of 9 layers with 20 neurons in each layer.

A summary of our results for this example is presented in figure 4. We observe that the *physics-informed neural network* is able to correctly identify the unknown parameters λ_1 and λ_2 with very high accuracy even when the training data was corrupted with noise. Specifically, for the case of noise-free training data, the error in estimating λ_1 and λ_2 is 0.078%, and 4.67%, respectively. The predictions remain robust even when the training data are corrupted with 1% uncorrelated Gaussian noise, returning an error of 0.17%, and 5.70%, for λ_1 and λ_2, respectively.

A more intriguing result stems from the network's ability to provide a qualitatively accurate prediction of the entire pressure field $p(t, x, y)$ in the absence of any training data on the pressure itself. A visual comparison against the exact pressure solution is presented in figure 4 for a representative pressure snapshot. Notice that the difference in magnitude between the exact and the predicted pressure is justified by the very nature of the *incompressible* Navier-Stokes system, as the pressure field is only identifiable up to a constant. This result of inferring a continuous quantity of interest from auxiliary measurements by leveraging the underlying physics is a great example of the enhanced capabilities that *physics-informed neural networks* have to offer, and highlights their potential in solving high-dimensional in-

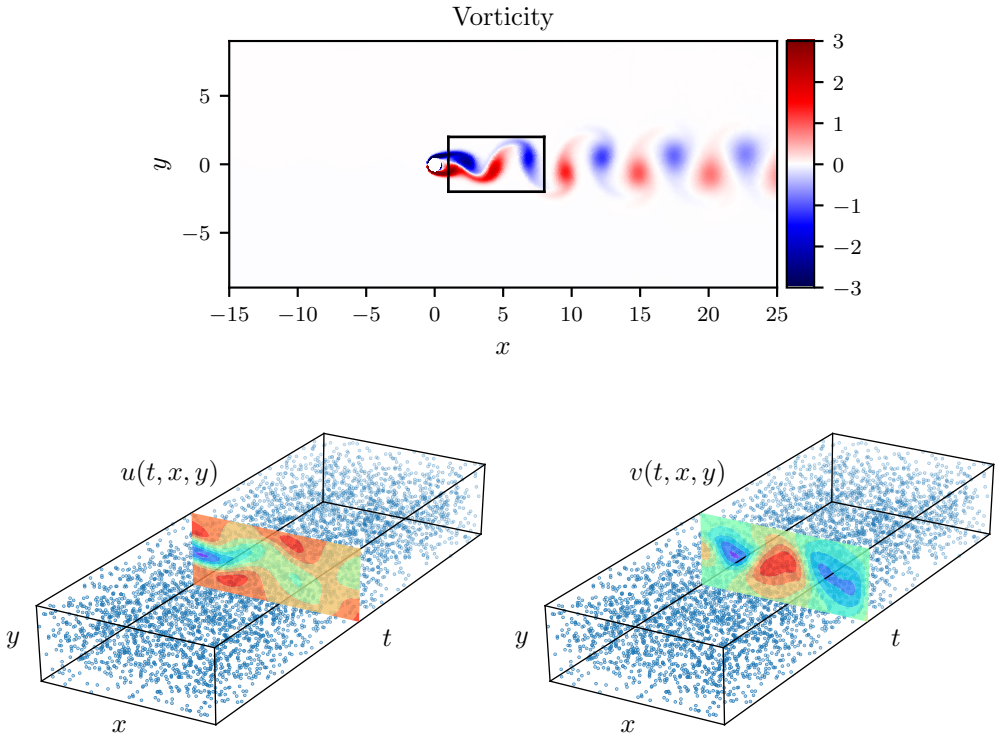

Figure 3: *Navier-Stokes equation: Top:* Incompressible flow and dynamic vortex shedding past a circular cylinder at $Re = 100$. The spatio-temporal training data correspond to the depicted rectangular region in the cylinder wake. *Bottom:* Locations of training data-points for the the stream-wise and transverse velocity components, $u(t, x, y)$ and $v(t, x, t)$, respectively.

verse problems.

Our approach so far assumes availability of scattered data throughout the entire spatio-temporal domain. However, in many cases of practical interest, one may only be able to observe the system at distinct time instants. In the next section, we introduce a different approach that tackles the data-driven discovery problem using only two data snapshots. We will see how, by leveraging the classical Runge-Kutta time-stepping schemes, one can construct discrete time *physics-informed neural networks* that can retain high predictive accuracy even when the temporal gap between the data snapshots is very large.

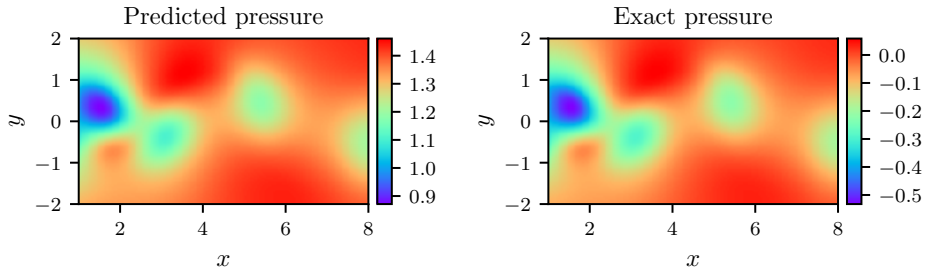

Correct PDE	$u_t + (uu_x + vu_y) = -p_x + 0.01(u_{xx} + u_{yy})$ $v_t + (uv_x + vv_y) = -p_y + 0.01(v_{xx} + v_{yy})$
Identified PDE (clean data)	$u_t + 0.999(uu_x + vu_y) = -p_x + 0.01047(u_{xx} + u_{yy})$ $v_t + 0.999(uv_x + vv_y) = -p_y + 0.01047(v_{xx} + v_{yy})$
Identified PDE (1% noise)	$u_t + 0.998(uu_x + vu_y) = -p_x + 0.01057(u_{xx} + u_{yy})$ $v_t + 0.998(uv_x + vv_y) = -p_y + 0.01057(v_{xx} + v_{yy})$

Figure 4: *Navier-Stokes equation: Top:* Predicted versus exact instantaneous pressure field $p(t, x, y)$ at a representative time instant. By definition, the pressure can be recovered up to a constant, hence justifying the different magnitude between the two plots. This remarkable qualitative agreement highlights the ability of *physics-informed neural networks* to identify the entire pressure field, despite the fact that no data on the pressure are used during model training. *Bottom:* Correct partial differential equation along with the identified one obtained by learning λ_1, λ_2 and $p(t, x, y)$.

4.2. Discrete Time Models

We begin by applying the general form of Runge-Kutta methods [45] with q stages to equation (1) and obtain

$$\begin{aligned} u^{n+c_i} &= u^n - \Delta t \textstyle\sum_{j=1}^{q} a_{ij} \mathcal{N}[u^{n+c_j}; \lambda], \quad i = 1, \ldots, q, \\ u^{n+1} &= u^n - \Delta t \textstyle\sum_{j=1}^{q} b_j \mathcal{N}[u^{n+c_j}; \lambda]. \end{aligned} \tag{20}$$

Here, $u^{n+c_j}(x) = u(t^n + c_j \Delta t, x)$ is the hidden state of the system at time $t^n + c_j \Delta t$ for $j = 1, \ldots, q$. This general form encapsulates both implicit and explicit time-stepping schemes, depending on the choice of the parameters $\{a_{ij}, b_j, c_j\}$. Equations (20) can be equivalently expressed as

$$\begin{aligned} u^n &= u_i^n, \quad i = 1, \ldots, q, \\ u^{n+1} &= u_i^{n+1}, \quad i = 1, \ldots, q. \end{aligned} \tag{21}$$

where

$$\begin{aligned} u_i^n &:= u^{n+c_i} + \Delta t \sum_{j=1}^{q} a_{ij} \mathcal{N}[u^{n+c_j}; \lambda], \quad i = 1, \ldots, q, \\ u_i^{n+1} &:= u^{n+c_i} + \Delta t \sum_{j=1}^{q} (a_{ij} - b_j) \mathcal{N}[u^{n+c_j}; \lambda], \quad i = 1, \ldots, q. \end{aligned} \tag{22}$$

We proceed by placing a multi-output neural network prior on

$$\left[u^{n+c_1}(x), \ldots, u^{n+c_q}(x)\right]. \tag{23}$$

This prior assumption along with equations (22) result in two *physics-informed neural networks*

$$\left[u_1^n(x), \ldots, u_q^n(x), u_{q+1}^n(x)\right], \tag{24}$$

and

$$\left[u_1^{n+1}(x), \ldots, u_q^{n+1}(x), u_{q+1}^{n+1}(x)\right]. \tag{25}$$

Given noisy measurements at two distinct temporal snapshots $\{\boldsymbol{x}^n, \boldsymbol{u}^n\}$ and $\{\boldsymbol{x}^{n+1}, \boldsymbol{u}^{n+1}\}$ of the system at times t^n and t^{n+1}, respectively, the shared parameters of the neural networks (23), (24), and (25) along with the parameters λ of the differential operator can be trained by minimizing the sum of squared errors

$$SSE = SSE_n + SSE_{n+1}, \tag{26}$$

where

$$SSE_n := \sum_{j=1}^{q} \sum_{i=1}^{N_n} |u_j^n(x^{n,i}) - u^{n,i}|^2,$$

and

$$SSE_{n+1} := \sum_{j=1}^{q} \sum_{i=1}^{N_{n+1}} |u_j^{n+1}(x^{n+1,i}) - u^{n+1,i}|^2.$$

Here, $\boldsymbol{x}^n = \{x^{n,i}\}_{i=1}^{N_n}$, $\boldsymbol{u}^n = \{u^{n,i}\}_{i=1}^{N_n}$, $\boldsymbol{x}^{n+1} = \{x^{n+1,i}\}_{i=1}^{N_{n+1}}$, and $\boldsymbol{u}^{n+1} = \{u^{n+1,i}\}_{i=1}^{N_{n+1}}$.

4.2.1. Example (Kortewegde Vries Equation)

Our final example aims to highlight the ability of the proposed framework to handle governing partial differential equations involving higher order derivatives. Here, we consider a mathematical model of waves on shallow water surfaces; the Korteweg-de Vries (KdV) equation. This equation can also be viewed as Burgers equation with an added dispersive term. The KdV

equation has several connections to physical problems. It describes the evolution of long one-dimensional waves in many physical settings. Such physical settings include shallow-water waves with weakly non-linear restoring forces, long internal waves in a density-stratified ocean, ion acoustic waves in a plasma, and acoustic waves on a crystal lattice. Moreover, the KdV equation is the governing equation of the string in the Fermi-Pasta-Ulam problem [48] in the continuum limit. The KdV equation reads as

$$u_t + \lambda_1 u u_x + \lambda_2 u_{xxx} = 0, \tag{27}$$

with (λ_1, λ_2) being the unknown parameters. For the KdV equation, the nonlinear operator in equations (22) is given by

$$\mathcal{N}[u^{n+c_j}] = \lambda_1 u^{n+c_j} u_x^{n+c_j} - \lambda_2 u_{xxx}^{n+c_j}$$

and the shared parameters of the neural networks (23), (24), and (25) along with the parameters $\lambda = (\lambda_1, \lambda_2)$ of the KdV equation can be learned by minimizing the sum of squared errors (26).

To obtain a set of training and test data we simulated (27) using conventional spectral methods. Specifically, starting from an initial condition $u(0, x) = \cos(\pi x)$ and assuming periodic boundary conditions, we have integrated equation (27) up to a final time $t = 1.0$ using the Chebfun package [40] with a spectral Fourier discretization with 512 modes and a fourth-order explicit Runge-Kutta temporal integrator with time-step $\Delta t = 10^{-6}$. Using this data-set, we then extract two solution snapshots at time $t^n = 0.2$ and $t^{n+1} = 0.8$, and randomly sub-sample them using $N_n = 199$ and $N_{n+1} = 201$ to generate a training data-set. We then use these data to train a discrete time *physics-informed neural network* by minimizing the sum of squared error loss of equation (26) using L-BFGS [35]. The network architecture used here comprises of 4 hidden layers, 50 neurons per layer, and an output layer predicting the solution at the q Runge-Kutta stages, i.e., $u^{n+c_j}(x)$, $j = 1, \ldots, q$, where q is empirically chosen to yield a temporal error accumulation of the order of machine precision ϵ by setting[4]

$$q = 0.5 \log \epsilon / \log(\Delta t), \tag{28}$$

[4]This is motivated by the theoretical error estimates for implicit Runge-Kutta schemes suggesting a truncation error of $\mathcal{O}(\Delta t^{2q})$ [45].

where the time-step for this example is $\Delta t = 0.6$.

The results of this experiment are summarized in figure 5. In the top panel, we present the exact solution $u(t, x)$, along with the locations of the two data snapshots used for training. A more detailed overview of the exact solution and the training data is given in the middle panel. It is worth noticing how the complex nonlinear dynamics of equation (27) causes dramatic differences in the form of the solution between the two reported snapshots. Despite these differences, and the large temporal gap between the two training snapshots, our method is able to correctly identify the unknown parameters regardless of whether the training data is corrupted with noise or not. Specifically, for the case of noise-free training data, the error in estimating λ_1 and λ_2 is 0.023%, and 0.006%, respectively, while the case with 1% noise in the training data returns errors of 0.057%, and 0.017%, respectively.

5. Conclusions

We have introduced *physics-informed neural networks*, a new class of universal function approximators that is capable of encoding any underlying physical laws that govern a given data-set, and can be described by partial differential equations. In this work, we design data-driven algorithms for inferring solutions to general nonlinear partial differential equations, and constructing computationally efficient physics-informed surrogate models. The resulting methods showcase a series of promising results for a diverse collection of problems in computational science, and open the path for endowing deep learning with the powerful capacity of mathematical physics to model the world around us. As deep learning technology is continuing to grow rapidly both in terms of methodological and algorithmic developments, we believe that this is a timely contribution that can benefit practitioners across a wide range of scientific domains. Specific applications that can readily enjoy these benefits include, but are not limited to, data-driven forecasting of physical processes, model predictive control, multi-physics/multi-scale modeling and simulation.

We must note however that the proposed methods should not be viewed as replacements of classical numerical methods for solving partial differential equations (e.g., finite elements, spectral methods, etc.). Such methods have matured over the last 50 years and, in many cases, meet the robustness and

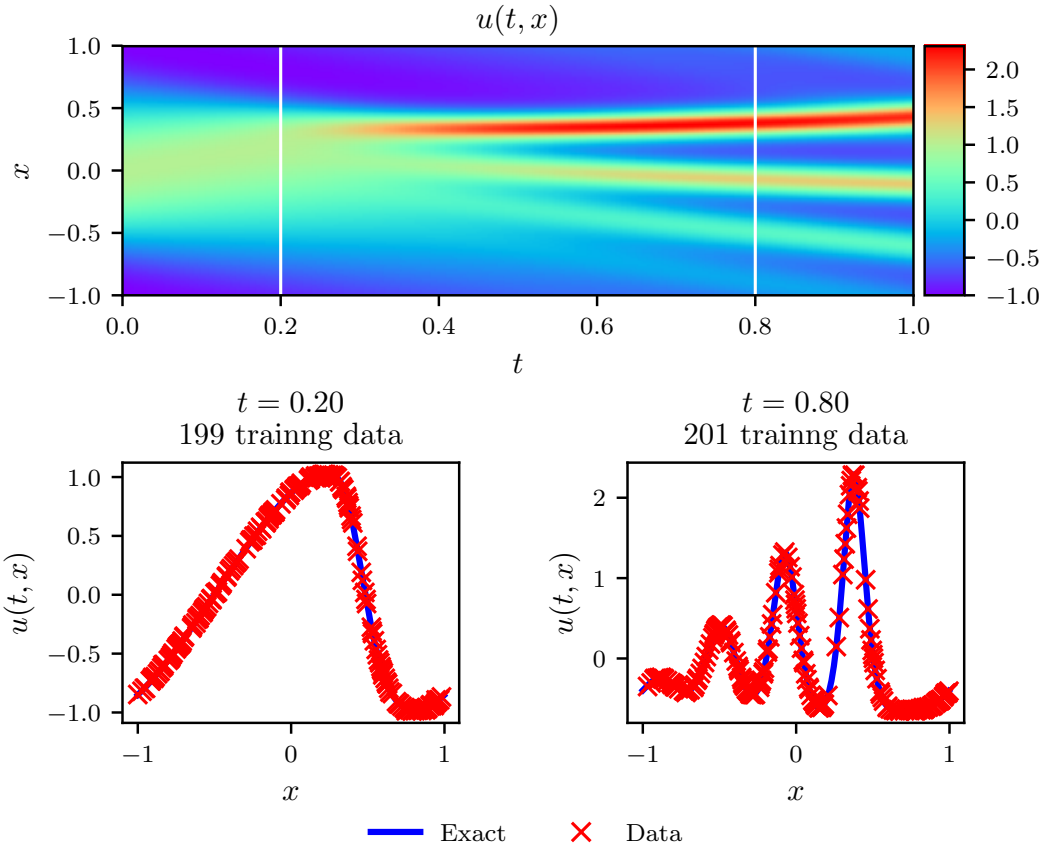

Correct PDE	$u_t + uu_x + 0.0025u_{xxx} = 0$
Identified PDE (clean data)	$u_t + 1.000uu_x + 0.0025002u_{xxx} = 0$
Identified PDE (1% noise)	$u_t + 0.999uu_x + 0.0024996u_{xxx} = 0$

Figure 5: *KdV equation: Top:* Solution $u(t,x)$ along with the temporal locations of the two training snapshots. *Middle:* Training data and exact solution corresponding to the two temporal snapshots depicted by the dashed vertical lines in the top panel. *Bottom:* Correct partial differential equation along with the identified one obtained by learning λ_1, λ_2.

computational efficiency standards required in practice. Our message here, as advocated in Section 3.2, is that classical methods such as the Runge-Kutta time-stepping schemes can coexist in harmony with deep neural networks, and offer invaluable intuition in constructing structured predictive

algorithms. Moreover, the implementation simplicity of the latter greatly favors rapid development and testing of new ideas, potentially opening the path for a new era in data-driven scientific computing.

Although a series of promising results was presented, the reader may perhaps agree this work creates more questions than it answers. How deep/wide should the neural network be? How much data is really needed? Why does the algorithm converge to unique values for the parameters of the differential operators, i.e., why is the algorithm not suffering from local optima for the parameters of the differential operator? Does the network suffer from vanishing gradients for deeper architectures and higher order differential operators? Could this be mitigated by using different activation functions? Can we improve on initializing the network weights or normalizing the data? Are the mean square error and the sum of squared errors the appropriate loss functions? Why are these methods seemingly so robust to noise in the data? How can we quantify the uncertainty associated with our predictions? Throughout this work, we have attempted to answer some of these questions, but we have observed that specific settings that yielded impressive results for one equation could fail for another. Admittedly, more work is needed collectively to set the foundations in this field.

In a broader context, and along the way of seeking answers to those questions, we believe that this work advocates a fruitful synergy between machine learning and classical computational physics that has the potential to enrich both fields and lead to high-impact developments.

Acknowledgements

This work received support by the DARPA EQUiPS grant N66001-15-2-4055 and the AFOSR grant FA9550-17-1-0013.

Appendix A. Data-driven solution of partial differential equations

This Appendix accompanies the main manuscript, and contains a series of systematic studies that aim to demonstrate the performance of the proposed algorithms for problems pertaining to *data-driven solution of partial differential equations*. Throughout this document, we will use the Burgers' equation as a canonical example.

Appendix A.1. Continuous Time Models

In one space dimension, the Burger's equation along with Dirichlet boundary conditions reads as

$$\begin{aligned} &u_t + uu_x - (0.01/\pi)u_{xx} = 0, \quad x \in [-1, 1], \quad t \in [0, 1], \\ &u(0, x) = -\sin(\pi x), \\ &u(t, -1) = u(t, 1) = 0. \end{aligned} \tag{A.1}$$

Let us define $f(t, x)$ to be given by

$$f := u_t + uu_x - (0.01/\pi)u_{xx},$$

and proceed by approximating $u(t, x)$ by a deep neural network. To highlight the simplicity in implementing this idea we have included a Python code snippet using Tensorflow [49]; currently one of the most popular and well documented open source libraries for machine learning computations. To this end, $u(t, x)$ can be simply defined as

```
def u(t, x):
    u = neural_net(tf.concat([t,x],1), weights, biases)
    return u
```

Correspondingly, the *physics-informed neural network* $f(t, x)$ takes the form

```
def f(t, x):
    u = u(t, x)
    u_t = tf.gradients(u, t)[0]
    u_x = tf.gradients(u, x)[0]
    u_xx = tf.gradients(u_x, x)[0]
    f = u_t + u*u_x - (0.01/tf.pi)*u_xx
    return f
```

The shared parameters between the neural networks $u(t, x)$ and $f(t, x)$ can be learned by minimizing the mean squared error loss

$$MSE = MSE_u + MSE_f, \tag{A.2}$$

where

$$MSE_u = \frac{1}{N_u} \sum_{i=1}^{N_u} |u(t_u^i, x_u^i) - u^i|^2,$$

and

$$MSE_f = \frac{1}{N_f}\sum_{i=1}^{N_f} |f(t_f^i, x_f^i)|^2.$$

Here, $\{t_u^i, x_u^i, u^i\}_{i=1}^{N_u}$ denote the initial and boundary training data on $u(t,x)$ and $\{t_f^i, x_f^i\}_{i=1}^{N_f}$ specify the collocations points for $f(t,x)$. The loss MSE_u corresponds to the initial and boundary data while MSE_f enforces the structure imposed by equation (A.1) at a finite set of collocation points. Although similar ideas for constraining neural networks using physical laws have been explored in previous studies [15, 16], here we revisit them using modern computational tools, and apply them to more challenging dynamic problems described by time-dependent nonlinear partial differential equations.

The Burgers equation is often considered as a prototype example of a hyperbolic conservation law (as $\nu \to 0$). Notice that if we want to "fabricate" an "exact" solution to this equation we would select a solution $u(t,x)$ (e.g., $e^{-t}\sin(\pi x)$) and obtain the corresponding right hand side $f(t,x)$ by differentiation. The resulting $u(t,x)$ and $f(t,x)$ are "guaranteed" to satisfy the Burgers equation and conserve all associated invariances by construction. In our work, we replace $u(t,x)$ by a neural network $u(t,x;W,b)$ and obtain a physics-informed neural network $f(t,x;W,b)$ by automatic differentiation. Consequently, the resulting pair $u(t,x;W,b)$ and $f(t,x;W,b)$ must satisfy the Burgers equation regardless of the choice of the weights W and bias b parameters. Hence, at this "prior" level, i.e. before we train the networks on a given set of data, our model should exactly preserves the continuity and momentum equations by construction. During training, given a data-set t_i, x_i, u_i and t_j, x_j, f_j, we then try to find the "correct" parameters W^* and b^* such that we get as good a fit as possible to both the observed data and the differential equation residual. During this process the residual, albeit small, will not be exactly zero, and therefore our approximation will conserve mass and momentum within the accuracy of the residual loss. Similar behavior is observed in classical Galerkin finite element methods, while the only numerical methods that are known to have exact conservation properties in this setting are discontinuous Galerkin and finite volumes.

In all benchmarks considered in this work, the total number of training data N_u is relatively small (a few hundred up to a few thousand points), and we chose to optimize all loss functions using L-BFGS a quasi-Newton, full-

batch gradient-based optimization algorithm [35]. For larger data-sets a more computationally efficient mini-batch setting can be readily employed using stochastic gradient descent and its modern variants [36, 37]. Despite the fact that there is no theoretical guarantee that this procedure converges to a global minimum, our empirical evidence indicates that, if the given partial differential equation is well-posed and its solution is unique, our method is capable of achieving good prediction accuracy given a sufficiently expressive neural network architecture and a sufficient number of collocation points N_f. This general observation deeply relates to the resulting optimization landscape induced by the mean square error loss of equation 4, and defines an open question for research that is in sync with recent theoretical developments in deep learning [38, 39]. Here, we will test the robustness of the proposed methodology using a series of systematic sensitivity studies that accompany the numerical results presented in the following.

Figure A.6 summarizes our results for the data-driven solution of the Burgers equation. Specifically, given a set of $N_u = 100$ randomly distributed initial and boundary data, we learn the latent solution $u(t, x)$ by training all 3021 parameters of a 9-layer deep neural network using the mean squared error loss of (A.2). Each hidden layer contained 20 neurons and a hyperbolic tangent activation function. The top panel of Figure A.6 shows the predicted spatio-temporal solution $u(t, x)$, along with the locations of the initial and boundary training data. We must underline that, unlike any classical numerical method for solving partial differential equations, this prediction is obtained without any sort of discretization of the spatio-temporal domain. The exact solution for this problem is analytically available [13], and the resulting prediction error is measured at $6.7 \cdot 10^{-4}$ in the relative $\mathbb{L}_2$-norm. Note that this error is about two orders of magnitude lower than the one reported in our previous work on data-driven solution of partial differential equation using Gaussian processes [8]. A more detailed assessment of the predicted solution is presented in the bottom panel of figure A.6. In particular, we present a comparison between the exact and the predicted solutions at different time instants $t = 0.25, 0.50, 0.75$. Using only a handful of initial and boundary data, the *physics-informed neural network* can accurately capture the intricate nonlinear behavior of the Burgers' equation that leads to the development of a sharp internal layer around $t = 0.4$. The latter is notoriously hard to accurately resolve with classical numerical methods and requires a laborious spatio-temporal discretization of equation (A.1).

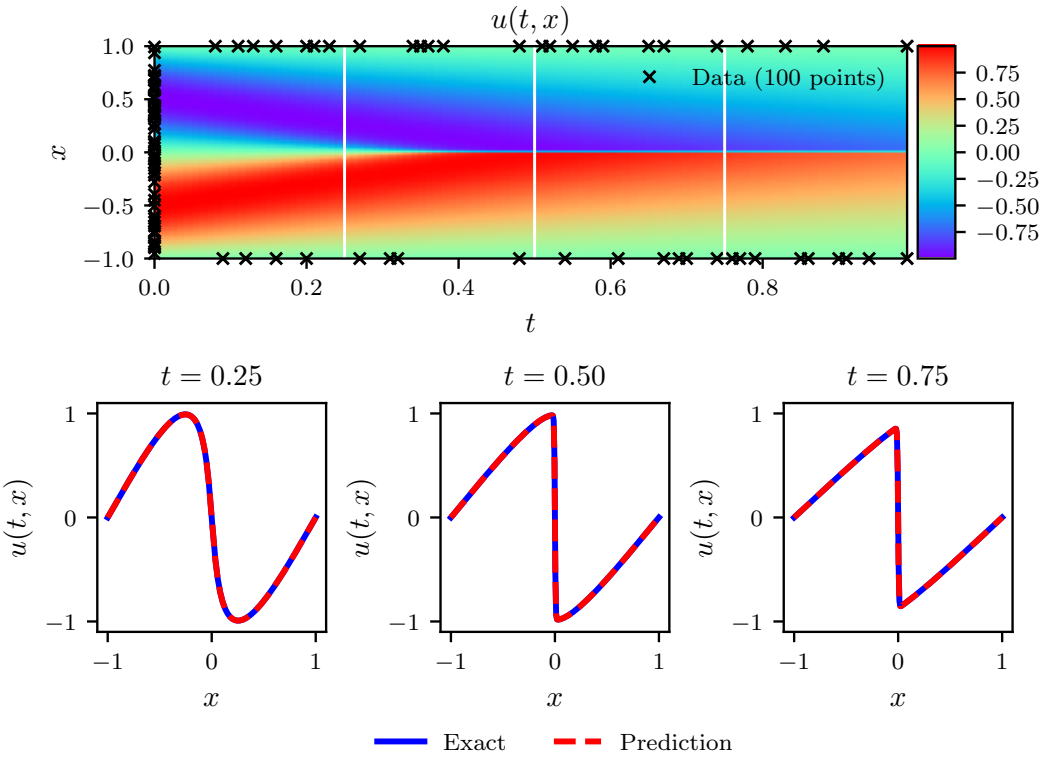

Figure A.6: *Burgers' equation: Top:* Predicted solution $u(t,x)$ along with the initial and boundary training data. In addition we are using 10,000 collocation points generated using a Latin Hypercube Sampling strategy. *Bottom:* Comparison of the predicted and exact solutions corresponding to the three temporal snapshots depicted by the white vertical lines in the top panel. The relative $\mathbb{L}_2$ error for this case is $6.7 \cdot 10^{-4}$. Model training took approximately 60 seconds on a single NVIDIA Titan X GPU card.

To further analyze the performance of our method, we have performed the following systematic studies to quantify its predictive accuracy for different number of training and collocation points, as well as for different neural network architectures. In table A.1 we report the resulting relative $\mathbb{L}_2$ error for different number of initial and boundary training data N_u and different number of collocation points N_f, while keeping the 9-layer network architecture fixed. The general trend shows increased prediction accuracy as the total number of training data N_u is increased, given a sufficient number of collocation points N_f. This observation highlights a key strength of *physics-informed neural networks*: by encoding the structure of the underlying phys-

N_u \ N_f	2000	4000	6000	7000	8000	10000
20	2.9e-01	4.4e-01	8.9e-01	1.2e+00	9.9e-02	4.2e-02
40	6.5e-02	1.1e-02	5.0e-01	9.6e-03	4.6e-01	7.5e-02
60	3.6e-01	1.2e-02	1.7e-01	5.9e-03	1.9e-03	8.2e-03
80	5.5e-03	1.0e-03	3.2e-03	7.8e-03	4.9e-02	4.5e-03
100	6.6e-02	2.7e-01	7.2e-03	6.8e-04	2.2e-03	6.7e-04
200	1.5e-01	2.3e-03	8.2e-04	8.9e-04	6.1e-04	4.9e-04

Table A.1: *Burgers' equation:* Relative $\mathbb{L}_2$ error between the predicted and the exact solution $u(t, x)$ for different number of initial and boundary training data N_u, and different number of collocation points N_f. Here, the network architecture is fixed to 9 layers with 20 neurons per hidden layer.

Layers \ Neurons	10	20	40
2	7.4e-02	5.3e-02	1.0e-01
4	3.0e-03	9.4e-04	6.4e-04
6	9.6e-03	1.3e-03	6.1e-04
8	2.5e-03	9.6e-04	5.6e-04

Table A.2: *Burgers' equation:* Relative $\mathbb{L}_2$ error between the predicted and the exact solution $u(t, x)$ for different number of hidden layers and different number of neurons per layer. Here, the total number of training and collocation points is fixed to $N_u = 100$ and $N_f = 10,000$, respectively.

ical law through the collocation points N_f, one can obtain a more accurate and data-efficient learning algorithm.[5] Finally, table A.2 shows the resulting relative $\mathbb{L}_2$ for different number of hidden layers, and different number of neurons per layer, while the total number of training and collocation points is kept fixed to $N_u = 100$ and $N_f = 10,000$, respectively. As expected, we observe that as the number of layers and neurons is increased (hence the capacity of the neural network to approximate more complex functions), the predictive accuracy is increased.

[5]Note that the case $N_f = 0$ corresponds to a standard neural network model, i.e., a neural network that does not take into account the underlying governing equation.

Appendix A.2. Discrete Time Models

Let us apply the general form of Runge-Kutta methods with q stages [45] to a general equation of the form

$$u_t + \mathcal{N}[u] = 0,\ x \in \Omega,\ t \in [0, T], \tag{A.3}$$

and obtain

$$\begin{aligned} u^{n+c_i} &= u^n - \Delta t \textstyle\sum_{j=1}^{q} a_{ij} \mathcal{N}[u^{n+c_j}], \quad i = 1, \ldots, q, \\ u^{n+1} &= u^n - \Delta t \textstyle\sum_{j=1}^{q} b_j \mathcal{N}[u^{n+c_j}]. \end{aligned} \tag{A.4}$$

Here, $u^{n+c_j}(x) = u(t^n + c_j \Delta t, x)$ for $j = 1, \ldots, q$. This general form encapsulates both implicit and explicit time-stepping schemes, depending on the choice of the parameters $\{a_{ij}, b_j, c_j\}$. Equations (7) can be equivalently expressed as

$$\begin{aligned} u^n &= u_i^n, \quad i = 1, \ldots, q, \\ u^n &= u_{q+1}^n, \end{aligned} \tag{A.5}$$

where

$$\begin{aligned} u_i^n &:= u^{n+c_i} + \Delta t \textstyle\sum_{j=1}^{q} a_{ij} \mathcal{N}[u^{n+c_j}], \quad i = 1, \ldots, q, \\ u_{q+1}^n &:= u^{n+1} + \Delta t \textstyle\sum_{j=1}^{q} b_j \mathcal{N}[u^{n+c_j}]. \end{aligned} \tag{A.6}$$

We proceed by placing a multi-output neural network prior on

$$\left[u^{n+c_1}(x), \ldots, u^{n+c_q}(x), u^{n+1}(x)\right]. \tag{A.7}$$

This prior assumption along with equations (A.6) result in a *physics-informed neural network* that takes x as an input and outputs

$$\left[u_1^n(x), \ldots, u_q^n(x), u_{q+1}^n(x)\right]. \tag{A.8}$$

To highlight the key features of the discrete time representation we revisit the problem of data-driven solution of the Burgers' equation. For this case, the nonlinear operator in equation (A.6) is given by

$$\mathcal{N}[u^{n+c_j}] = u^{n+c_j} u_x^{n+c_j} - (0.01/\pi) u_{xx}^{n+c_j},$$

and the shared parameters of the neural networks (A.7) and (A.8) can be learned by minimizing the sum of squared errors

$$SSE = SSE_n + SSE_b, \tag{A.9}$$

where

$$SSE_n = \sum_{j=1}^{q+1} \sum_{i=1}^{N_n} |u_j^n(x^{n,i}) - u^{n,i}|^2,$$

and

$$SSE_b = \sum_{i=1}^{q} \left(|u^{n+c_i}(-1)|^2 + |u^{n+c_i}(1)|^2 \right) + |u^{n+1}(-1)|^2 + |u^{n+1}(1)|^2.$$

Here, $\{x^{n,i}, u^{n,i}\}_{i=1}^{N_n}$ corresponds to the data at time t^n. The Runge-Kutta scheme now allows us to infer the latent solution $u(t, x)$ in a sequential fashion. Starting from initial data $\{x^{n,i}, u^{n,i}\}_{i=1}^{N_n}$ at time t^n and data at the domain boundaries $x = -1$ and $x = 1$, we can use the aforementioned loss function (A.9) to train the networks of (A.7), (A.8), and predict the solution at time t^{n+1}. A Runge-Kutta time-stepping scheme would then use this prediction as initial data for the next step and proceed to train again and predict $u(t^{n+2}, x)$, $u(t^{n+3}, x)$, etc., one step at a time.

The result of applying this process to the Burgers' equation is presented in figure A.7. For illustration purposes, we start with a set of $N_n = 250$ initial data at $t = 0.1$, and employ a *physics-informed neural network* induced by an implicit Runge-Kutta scheme with 500 stages to predict the solution at time $t = 0.9$ in a single step. The theoretical error estimates for this scheme predict a temporal error accumulation of $\mathcal{O}(\Delta t^{2q})$ [45], which in our case translates into an error way below machine precision, i.e., $\Delta t^{2q} = 0.8^{1000} \approx 10^{-97}$. To our knowledge, this is the first time that an implicit Runge-Kutta scheme of that high-order has ever been used. Remarkably, starting from smooth initial data at $t = 0.1$ we can predict the nearly discontinuous solution at $t = 0.9$ in a single time-step with a relative $\mathbb{L}_2$ error of $8.2 \cdot 10^{-4}$. This error is two orders of magnitude lower that the one reported in [8], and it is entirely attributed to the neural network's capacity to approximate $u(t, x)$, as well as to the degree that the sum of squared errors loss allows interpolation of the training data. The network architecture used here consists of 4 layers with 50 neurons in each hidden layer.

A detailed systematic study to quantify the effect of different network architectures is presented in table A.5. By keeping the number of Runge-Kutta stages fixed to $q = 500$ and the time-step size to $\Delta t = 0.8$, we have

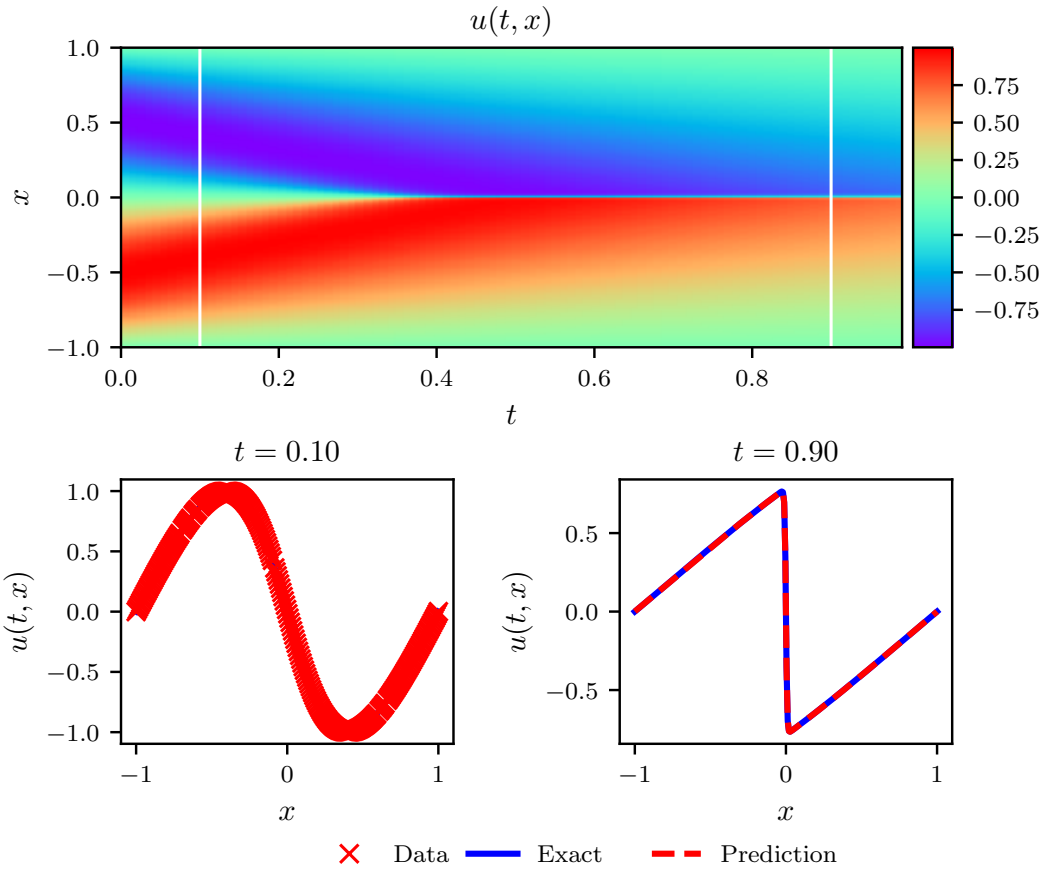

Figure A.7: *Burgers equation: Top:* Solution $u(t,x)$ along with the location of the initial training snapshot at $t = 0.1$ and the final prediction snapshot at $t = 0.9$. *Bottom:* Initial training data and final prediction at the snapshots depicted by the white vertical lines in the top panel. The relative $\mathbb{L}_2$ error for this case is $8.2 \cdot 10^{-4}$.

varied the number of hidden layers and the number of neurons per layer, and monitored the resulting relative $\mathbb{L}_2$ error for the predicted solution at time $t = 0.9$. Evidently, as the neural network capacity is increased the predictive accuracy is enhanced.

The key parameters controlling the performance of our discrete time algorithm are the total number of Runge-Kutta stages q and the time-step size Δt. In table A.4 we summarize the results of an extensive systematic study where we fix the network architecture to 4 hidden layers with 50 neurons

Layers \ Neurons	10	25	50
1	4.1e-02	4.1e-02	1.5e-01
2	2.7e-03	5.0e-03	2.4e-03
3	3.6e-03	1.9e-03	9.5e-04

Table A.3: *Burgers' equation:* Relative final prediction error measure in the $\mathbb{L}_2$ norm for different number of hidden layers and neurons in each layer. Here, the number of Runge-Kutta stages is fixed to 500 and the time-step size to $\Delta t = 0.8$.

per layer, and vary the number of Runge-Kutta stages q and the time-step size Δt. Specifically, we see how cases with low numbers of stages fail to yield accurate results when the time-step size is large. For instance, the case $q = 1$ corresponding to the classical trapezoidal rule, and the case $q = 2$ corresponding to the 4^{th}-order Gauss-Legendre method, cannot retain their predictive accuracy for time-steps larger than 0.2, thus mandating a solution strategy with multiple time-steps of small size. On the other hand, the ability to push the number of Runge-Kutta stages to 32 and even higher allows us to take very large time steps, and effectively resolve the solution in a single step without sacrificing the accuracy of our predictions. Moreover, numerical stability is not sacrificed either as implicit Gauss-Legendre is the only family of time-stepping schemes that remain A-stable regardless of their order, thus making them ideal for stiff problems [45]. These properties are unprecedented for an algorithm of such implementation simplicity, and illustrate one of the key highlights of our discrete time approach.

Finally, in table A.5 we provide a systematic study to quantify the accuracy of the predicted solution as we vary the spatial resolution of the input data. As expected, increasing the total number of training data results in enhanced prediction accuracy.

Appendix B. Data-driven discovery of partial differential equations

This Appendix accompanies the main manuscript, and contains a series of systematic studies that aim to demonstrate the performance of the proposed algorithms for problems pertaining to *data-driven discovery of partial differential equations*. Throughout this document, we will use the Burgers' equation as a canonical example.

q \ Δt	0.2	0.4	0.6	0.8
1	3.5e-02	1.1e-01	2.3e-01	3.8e-01
2	5.4e-03	5.1e-02	9.3e-02	2.2e-01
4	1.2e-03	1.5e-02	3.6e-02	5.4e-02
8	6.7e-04	1.8e-03	8.7e-03	5.8e-02
16	5.1e-04	7.6e-02	8.4e-04	1.1e-03
32	7.4e-04	5.2e-04	4.2e-04	7.0e-04
64	4.5e-04	4.8e-04	1.2e-03	7.8e-04
100	5.1e-04	5.7e-04	1.8e-02	1.2e-03
500	4.1e-04	3.8e-04	4.2e-04	8.2e-04

Table A.4: *Burgers' equation:* Relative final prediction error measured in the $\mathbb{L}_2$ norm for different number of Runge-Kutta stages q and time-step sizes Δt. Here, the network architecture is fixed to 4 hidden layers with 50 neurons in each layer.

N	250	200	150	100	50	10
Error	4.02e-4	2.93e-3	9.39e-3	5.54e-2	1.77e-2	7.58e-1

Table A.5: *Burgers equation:* Relative $\mathcal{L}_2$ error between the predicted and the exact solution $u(t, x)$ for different number of training data N_n. Here, we have fixed $q = 500$, and used a neural network architecture with 3 hidden layers and 50 neurons per hidden layer.

Appendix B.1. Continuous Time Models

As a first example, let us consider the Burgers' equation. This equation arises in various areas of applied mathematics, including fluid mechanics, nonlinear acoustics, gas dynamics, and traffic flow [13]. It is a fundamental partial differential equation and can be derived from the Navier-Stokes equations for the velocity field by dropping the pressure gradient term. For small values of the viscosity parameters, Burgers' equation can lead to shock formation that is notoriously hard to resolve by classical numerical methods. In one space dimension the equation reads as

$$u_t + \lambda_1 u u_x - \lambda_2 u_{xx} = 0. \tag{B.1}$$

Let us define $f(t, x)$ to be given by

$$f := u_t + \lambda_1 u u_x - \lambda_2 u_{xx}, \tag{B.2}$$

and proceed by approximating $u(t, x)$ by a deep neural network. This will result in the *physics-informed neural network* $f(t, x)$. The shared parameters

of the neural networks $u(t,x)$ and $f(t,x)$ along with the parameters $\lambda = (\lambda_1, \lambda_2)$ of the differential operator can be learned by minimizing the mean squared error loss

$$MSE = MSE_u + MSE_f, \tag{B.3}$$

where

$$MSE_u = \frac{1}{N}\sum_{i=1}^{N} |u(t_u^i, x_u^i) - u^i|^2,$$

and

$$MSE_f = \frac{1}{N}\sum_{i=1}^{N} |f(t_u^i, x_u^i)|^2.$$

Here, $\{t_u^i, x_u^i, u^i\}_{i=1}^N$ denote the training data on $u(t,x)$. The loss MSE_u corresponds to the training data on $u(t,x)$ while MSE_f enforces the structure imposed by equation (B.1) at a finite set of collocation points, whose number and location is taken to be the same as the training data.

To illustrate the effectiveness of our approach, we have created a training data-set by randomly generating $N = 2,000$ points across the entire spatio-temporal domain from the exact solution corresponding to $\lambda_1 = 1.0$ and $\lambda_2 = 0.01/\pi$. The locations of the training points are illustrated in the top panel of figure B.8. This data-set is then used to train a 9-layer deep neural network with 20 neurons per hidden layer by minimizing the mean square error loss of (B.3) using the L-BFGS optimizer [35]. Upon training, the network is calibrated to predict the entire solution $u(t,x)$, as well as the unknown parameters $\lambda = (\lambda_1, \lambda_2)$ that define the underlying dynamics. A visual assessment of the predictive accuracy of the *physics-informed neural network* is given in the middle and bottom panels of figure B.8. The network is able to identify the underlying partial differential equation with remarkable accuracy, even in the case where the scattered training data is corrupted with 1% uncorrelated noise.

To further scrutinize the performance of our algorithm, we have performed a systematic study with respect to the total number of training data, the noise corruption levels, and the neural network architecture. The results are summarized in tables B.6 and B.7. The key observation here is that the proposed methodology appears to be very robust with respect to noise levels in the data, and yields a reasonable identification accuracy even for noise

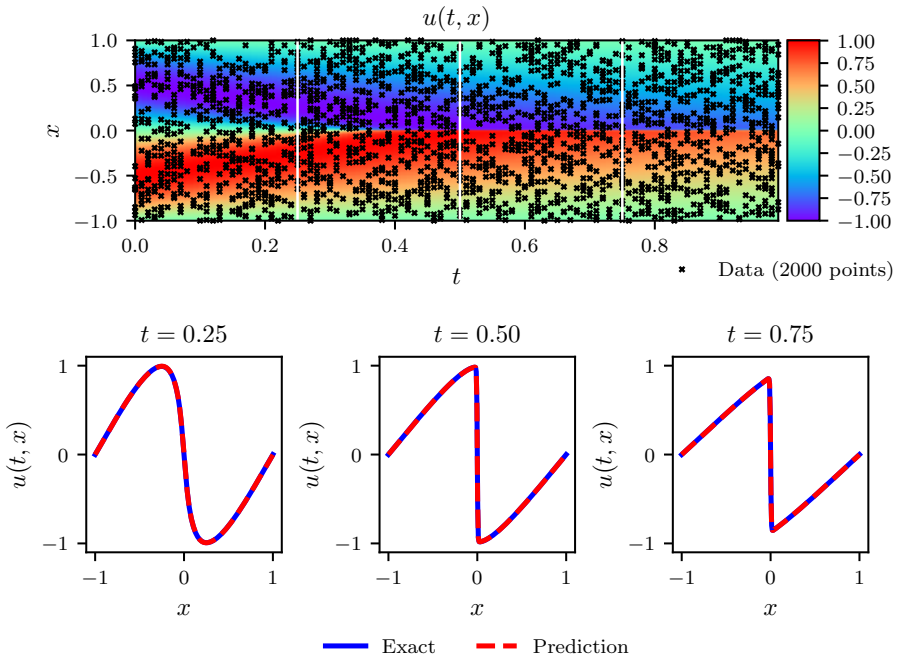

Correct PDE	$u_t + uu_x - 0.0031831u_{xx} = 0$
Identified PDE (clean data)	$u_t + 0.99915uu_x - 0.0031794u_{xx} = 0$
Identified PDE (1% noise)	$u_t + 1.00042uu_x - 0.0032098u_{xx} = 0$

Figure B.8: *Burgers equation: Top:* Predicted solution $u(t,x)$ along with the training data. *Middle:* Comparison of the predicted and exact solutions corresponding to the three temporal snapshots depicted by the dashed vertical lines in the top panel. *Bottom:* Correct partial differential equation along with the identified one obtained by learning λ_1 and λ_2.

corruption up to 10%. This enhanced robustness seems to greatly outperform competing approaches using Gaussian process regression as previously reported in [9] as well as approaches relying on sparse regression that require relatively clean data for accurately computing numerical gradients [50]. We also observe some variability and non monotonic trends in tables B.6 and B.7 as the network architecture and total number of training points are changed. This variability could be potentially attributed to different factors pertaining to the equation itself as well as the particular neural network setup, and gives rise to a series of questions that require further investigation, as discussed in the concluding remarks section of this paper.

	% error in λ_1				% error in λ_2			
noise / N_u	0%	1%	5%	10%	0%	1%	5%	10%
500	0.131	0.518	0.118	1.319	13.885	0.483	1.708	4.058
1000	0.186	0.533	0.157	1.869	3.719	8.262	3.481	14.544
1500	0.432	0.033	0.706	0.725	3.093	1.423	0.502	3.156
2000	0.096	0.039	0.190	0.101	0.469	0.008	6.216	6.391

Table B.6: *Burgers' equation:* Percentage error in the identified parameters λ_1 and λ_2 for different number of training data N corrupted by different noise levels. Here, the neural network architecture is kept fixed to 9 layers and 20 neurons per layer.

	% error in λ_1			% error in λ_2		
Layers / Neurons	10	20	40	10	20	40
2	11.696	2.837	1.679	103.919	67.055	49.186
4	0.332	0.109	0.428	4.721	1.234	6.170
6	0.668	0.629	0.118	3.144	3.123	1.158
8	0.414	0.141	0.266	8.459	1.902	1.552

Table B.7: *Burgers' equation:* Percentage error in the identified parameters λ_1 and λ_2 for different number of hidden layers and neurons per layer. Here, the training data is considered to be noise-free and fixed to $N = 2,000$.

Appendix B.2. Discrete Time Models

Our starting point here is similar to as described in section 3.2. Now equations (7) can be equivalently expressed as

$$\begin{aligned} u^n &= u_i^n, \quad i = 1, \ldots, q, \\ u^{n+1} &= u_i^{n+1}, \quad i = 1, \ldots, q. \end{aligned} \tag{B.4}$$

where

$$\begin{aligned} u_i^n &:= u^{n+c_i} + \Delta t \textstyle\sum_{j=1}^q a_{ij} \mathcal{N}[u^{n+c_j}; \lambda], \quad i = 1, \ldots, q, \\ u_i^{n+1} &:= u^{n+c_i} + \Delta t \textstyle\sum_{j=1}^q (a_{ij} - b_j) \mathcal{N}[u^{n+c_j}; \lambda], \quad i = 1, \ldots, q. \end{aligned} \tag{B.5}$$

We proceed by placing a multi-output neural network prior on

$$\left[u^{n+c_1}(x), \ldots, u^{n+c_q}(x)\right]. \tag{B.6}$$

This prior assumption along with equations (22) result in two *physics-informed neural networks*

$$\left[u_1^n(x), \ldots, u_q^n(x), u_{q+1}^n(x)\right], \tag{B.7}$$

and

$$\left[u_1^{n+1}(x), \ldots, u_q^{n+1}(x), u_{q+1}^{n+1}(x)\right]. \tag{B.8}$$

Given noisy measurements at two distinct temporal snapshots $\{\boldsymbol{x}^n, \boldsymbol{u}^n\}$ and $\{\boldsymbol{x}^{n+1}, \boldsymbol{u}^{n+1}\}$ of the system at times t^n and t^{n+1}, respectively, the shared parameters of the neural networks (B.6), (B.7), and (B.8) along with the parameters λ of the differential operator can be trained by minimizing the sum of squared errors

$$SSE = SSE_n + SSE_{n+1}, \tag{B.9}$$

where

$$SSE_n := \sum_{j=1}^{q} \sum_{i=1}^{N_n} |u_j^n(x^{n,i}) - u^{n,i}|^2,$$

and

$$SSE_{n+1} := \sum_{j=1}^{q} \sum_{i=1}^{N_{n+1}} |u_j^{n+1}(x^{n+1,i}) - u^{n+1,i}|^2.$$

Here, $\boldsymbol{x}^n = \{x^{n,i}\}_{i=1}^{N_n}$, $\boldsymbol{u}^n = \{u^{n,i}\}_{i=1}^{N_n}$, $\boldsymbol{x}^{n+1} = \{x^{n+1,i}\}_{i=1}^{N_{n+1}}$, and $\boldsymbol{u}^{n+1} = \{u^{n+1,i}\}_{i=1}^{N_{n+1}}$.

Appendix B.3. Example (Burgers' Equation)

Let us illustrate the key features of this method through the lens of the Burgers' equation. Recall the equation's form

$$u_t + \lambda_1 u u_x - \lambda_2 u_{xx} = 0, \tag{B.10}$$

and notice that the nonlinear spatial operator in equation (B.5) is given by

$$\mathcal{N}[u^{n+c_j}] = \lambda_1 u^{n+c_j} u_x^{n+c_j} - \lambda_2 u_{xx}^{n+c_j}.$$

Given merely two training data snapshots, the shared parameters of the neural networks (B.6), (B.7), and (B.8) along with the parameters $\lambda = (\lambda_1, \lambda_2)$ of the Burgers' equation can be learned by minimizing the sum of squared errors in equation (B.9). Here, we have created a training data-set comprising of $N_n = 199$ and $N_{n+1} = 201$ spatial points by randomly sampling the

exact solution at time instants $t^n = 0.1$ and $t^{n+1} = 0.9$, respectively. The training data are shown in the top and middle panel of figure B.9. The neural network architecture used here consists of 4 hidden layers with 50 neurons each, while the number of Runge-Kutta stages is empirically chosen to yield a temporal error accumulation of the order of machine precision ϵ by setting[6]

$$q = 0.5 \log \epsilon / \log(\Delta t), \tag{B.11}$$

where the time-step for this example is $\Delta t = 0.8$. The bottom panel of figure B.9 summarizes the identified parameters $\lambda = (\lambda_1, \lambda_2)$ for the cases of noise-free data, as well as noisy data with 1% of Gaussian uncorrelated noise corruption. For both cases, the proposed algorithm is able to learn the correct parameter values $\lambda_1 = 1.0$ and $\lambda_2 = 0.01/\pi$ with remarkable accuracy, despite the fact that the two data snapshots used for training are very far apart, and potentially describe different regimes of the underlying dynamics.

A sensitivity analysis is performed to quantify the accuracy of our predictions with respect to the gap between the training snapshots Δt, the noise levels in the training data, and the *physics-informed neural network* architecture. As shown in table B.8, the proposed algorithm is quite robust to both Δt and the noise corruption levels, and it returns reasonable estimates for the unknown parameters. This robustness is mainly attributed to the flexibility of the underlying implicit Runge-Kutta scheme to admit an arbitrarily high number of stages, allowing the data snapshots to be very far apart in time, while not compromising the accuracy with which the nonlinear dynamics of equation (B.10) are resolved. This is the key highlight of our discrete time formulation for identification problems, setting it apart from competing approaches [9, 50]. Lastly, table B.9 presents the percentage error in the identified parameters, demonstrating the robustness of our estimates with respect to the underlying neural network architecture. Despite the overall positive results, the variability observed in tables B.8 and B.9 is still largely unexplained and naturally motivates a series of questions provided in the concluding remarks section of this paper.

[6]This is motivated by the theoretical error estimates for implicit Runge-Kutta schemes suggesting a truncation error of $\mathcal{O}(\Delta t^{2q})$ [45].

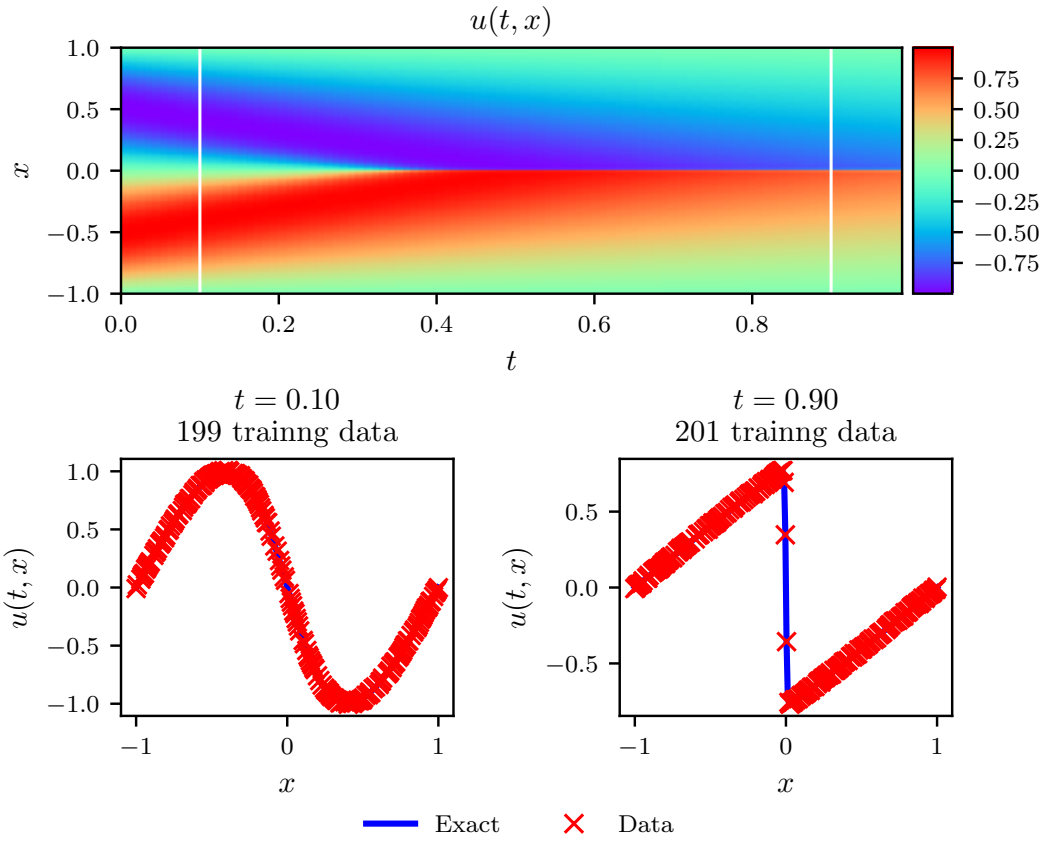

Correct PDE	$u_t + uu_x + 0.003183u_{xx} = 0$
Identified PDE (clean data)	$u_t + 1.000uu_x + 0.003193u_{xx} = 0$
Identified PDE (1% noise)	$u_t + 1.000uu_x + 0.003276u_{xx} = 0$

Figure B.9: *Burgers equation: Top:* Solution $u(t,x)$ along with the temporal locations of the two training snapshots. *Middle:* Training data and exact solution corresponding to the two temporal snapshots depicted by the dashed vertical lines in the top panel. *Bottom:* Correct partial differential equation along with the identified one obtained by learning λ_1, λ_2.

References

[1] A. Krizhevsky, I. Sutskever, G. E. Hinton, Imagenet classification with deep convolutional neural networks, in: Advances in neural information processing systems, pp. 1097–1105.

	% error in λ_1				% error in λ_2			
Δt \ noise	0%	1%	5%	10%	0%	1%	5%	10%
0.2	0.002	0.435	6.073	3.273	0.151	4.982	59.314	83.969
0.4	0.001	0.119	1.679	2.985	0.088	2.816	8.396	8.377
0.6	0.002	0.064	2.096	1.383	0.090	0.068	3.493	24.321
0.8	0.010	0.221	0.097	1.233	1.918	3.215	13.479	1.621

Table B.8: *Burgers' equation:* Percentage error in the identified parameters λ_1 and λ_2 for different gap size Δt between two different snapshots and for different noise levels.

	% error in λ_1			% error in λ_2		
Layers \ Neurons	10	25	50	10	25	50
1	1.868	4.868	1.960	180.373	237.463	123.539
2	0.443	0.037	0.015	29.474	2.676	1.561
3	0.123	0.012	0.004	7.991	1.906	0.586
4	0.012	0.020	0.011	1.125	4.448	2.014

Table B.9: *Burgers' equation:* Percentage error in the identified parameters λ_1 and λ_2 for different number of hidden layers and neurons in each layer.

[2] B. M. Lake, R. Salakhutdinov, J. B. Tenenbaum, Human-level concept learning through probabilistic program induction, Science 350 (2015) 1332–1338.

[3] B. Alipanahi, A. Delong, M. T. Weirauch, B. J. Frey, Predicting the sequence specificities of DNA-and RNA-binding proteins by deep learning, Nature biotechnology 33 (2015) 831–838.

[4] M. Raissi, P. Perdikaris, G. E. Karniadakis, Inferring solutions of differential equations using noisy multi-fidelity data, Journal of Computational Physics 335 (2017) 736–746.

[5] M. Raissi, P. Perdikaris, G. E. Karniadakis, Machine learning of linear differential equations using Gaussian processes, Journal of Computational Physics 348 (2017) 683 – 693.

[6] H. Owhadi, Bayesian numerical homogenization, Multiscale Modeling & Simulation 13 (2015) 812–828.

[7] C. E. Rasmussen, C. K. Williams, Gaussian processes for machine learning, volume 1, MIT press Cambridge, 2006.

[8] M. Raissi, P. Perdikaris, G. E. Karniadakis, Numerical Gaussian processes for time-dependent and non-linear partial differential equations, arXiv preprint arXiv:1703.10230 (2017).

[9] M. Raissi, G. E. Karniadakis, Hidden physics models: Machine learning of nonlinear partial differential equations, arXiv preprint arXiv:1708.00588 (2017).

[10] H. Owhadi, C. Scovel, T. Sullivan, et al., Brittleness of Bayesian inference under finite information in a continuous world, Electronic Journal of Statistics 9 (2015) 1–79.

[11] K. Hornik, M. Stinchcombe, H. White, Multilayer feedforward networks are universal approximators, Neural networks 2 (1989) 359–366.

[12] A. G. Baydin, B. A. Pearlmutter, A. A. Radul, J. M. Siskind, Automatic differentiation in machine learning: a survey, arXiv preprint arXiv:1502.05767 (2015).

[13] C. Basdevant, M. Deville, P. Haldenwang, J. Lacroix, J. Ouazzani, R. Peyret, P. Orlandi, A. Patera, Spectral and finite difference solutions of the Burgers equation, Computers & fluids 14 (1986) 23–41.

[14] S. H. Rudy, S. L. Brunton, J. L. Proctor, J. N. Kutz, Data-driven discovery of partial differential equations, Science Advances 3 (2017).

[15] I. E. Lagaris, A. Likas, D. I. Fotiadis, Artificial neural networks for solving ordinary and partial differential equations, IEEE Transactions on Neural Networks 9 (1998) 987–1000.

[16] D. C. Psichogios, L. H. Ungar, A hybrid neural network-first principles approach to process modeling, AIChE Journal 38 (1992) 1499–1511.

[17] J.-X. Wang, J. Wu, J. Ling, G. Iaccarino, H. Xiao, A comprehensive physics-informed machine learning framework for predictive turbulence modeling, arXiv preprint arXiv:1701.07102 (2017).

[18] Y. Zhu, N. Zabaras, Bayesian deep convolutional encoder-decoder networks for surrogate modeling and uncertainty quantification, arXiv preprint arXiv:1801.06879 (2018).

[19] T. Hagge, P. Stinis, E. Yeung, A. M. Tartakovsky, Solving differential equations with unknown constitutive relations as recurrent neural networks, arXiv preprint arXiv:1710.02242 (2017).

[20] R. Tripathy, I. Bilionis, Deep UQ: Learning deep neural network surrogate models for high dimensional uncertainty quantification, arXiv preprint arXiv:1802.00850 (2018).

[21] P. R. Vlachas, W. Byeon, Z. Y. Wan, T. P. Sapsis, P. Koumoutsakos, Data-driven forecasting of high-dimensional chaotic systems with long-short term memory networks, arXiv preprint arXiv:1802.07486 (2018).

[22] E. J. Parish, K. Duraisamy, A paradigm for data-driven predictive modeling using field inversion and machine learning, Journal of Computational Physics 305 (2016) 758–774.

[23] K. Duraisamy, Z. J. Zhang, A. P. Singh, New approaches in turbulence and transition modeling using data-driven techniques, in: 53rd AIAA Aerospace Sciences Meeting, p. 1284.

[24] J. Ling, A. Kurzawski, J. Templeton, Reynolds averaged turbulence modelling using deep neural networks with embedded invariance, Journal of Fluid Mechanics 807 (2016) 155–166.

[25] Z. J. Zhang, K. Duraisamy, Machine learning methods for data-driven turbulence modeling, in: 22nd AIAA Computational Fluid Dynamics Conference, p. 2460.

[26] M. Milano, P. Koumoutsakos, Neural network modeling for near wall turbulent flow, Journal of Computational Physics 182 (2002) 1–26.

[27] P. Perdikaris, D. Venturi, G. E. Karniadakis, Multifidelity information fusion algorithms for high-dimensional systems and massive data sets, SIAM J. Sci. Comput. 38 (2016) B521–B538.

[28] R. Rico-Martinez, J. Anderson, I. Kevrekidis, Continuous-time nonlinear signal processing: a neural network based approach for gray box

identification, in: Neural Networks for Signal Processing [1994] IV. Proceedings of the 1994 IEEE Workshop, IEEE, pp. 596–605.

[29] J. Ling, J. Templeton, Evaluation of machine learning algorithms for prediction of regions of high reynolds averaged navier stokes uncertainty, Physics of Fluids 27 (2015) 085103.

[30] H. W. Lin, M. Tegmark, D. Rolnick, Why does deep and cheap learning work so well?, Journal of Statistical Physics 168 (2017) 1223–1247.

[31] R. Kondor, N-body networks: a covariant hierarchical neural network architecture for learning atomic potentials, arXiv preprint arXiv:1803.01588 (2018).

[32] R. Kondor, S. Trivedi, On the generalization of equivariance and convolution in neural networks to the action of compact groups, arXiv preprint arXiv:1802.03690 (2018).

[33] M. Hirn, S. Mallat, N. Poilvert, Wavelet scattering regression of quantum chemical energies, Multiscale Modeling & Simulation 15 (2017) 827–863.

[34] S. Mallat, Understanding deep convolutional networks, Phil. Trans. R. Soc. A 374 (2016) 20150203.

[35] D. C. Liu, J. Nocedal, On the limited memory BFGS method for large scale optimization, Mathematical programming 45 (1989) 503–528.

[36] I. Goodfellow, Y. Bengio, A. Courville, Deep learning, MIT press, 2016.

[37] D. Kingma, J. Ba, Adam: A method for stochastic optimization, arXiv preprint arXiv:1412.6980 (2014).

[38] A. Choromanska, M. Henaff, M. Mathieu, G. B. Arous, Y. LeCun, The loss surfaces of multilayer networks, in: Artificial Intelligence and Statistics, pp. 192–204.

[39] R. Shwartz-Ziv, N. Tishby, Opening the black box of deep neural networks via information, arXiv preprint arXiv:1703.00810 (2017).

[40] T. A. Driscoll, N. Hale, L. N. Trefethen, Chebfun guide, 2014.

[41] M. Stein, Large sample properties of simulations using latin hypercube sampling, Technometrics 29 (1987) 143–151.

[42] J. Snoek, H. Larochelle, R. P. Adams, Practical bayesian optimization of machine learning algorithms, in: Advances in neural information processing systems, pp. 2951–2959.

[43] H.-J. Bungartz, M. Griebel, Sparse grids, Acta numerica 13 (2004) 147–269.

[44] I. H. Sloan, H. Woźniakowski, When are quasi-monte carlo algorithms efficient for high dimensional integrals?, Journal of Complexity 14 (1998) 1–33.

[45] A. Iserles, A first course in the numerical analysis of differential equations, 44, Cambridge University Press, 2009.

[46] T. Von Kármán, Aerodynamics, volume 9, McGraw-Hill New York, 1963.

[47] G. Karniadakis, S. Sherwin, Spectral/hp element methods for computational fluid dynamics, Oxford University Press, 2013.

[48] T. Dauxois, Fermi, Pasta, Ulam and a mysterious lady, arXiv preprint arXiv:0801.1590 (2008).

[49] M. Abadi, A. Agarwal, P. Barham, E. Brevdo, Z. Chen, C. Citro, G. S. Corrado, A. Davis, J. Dean, M. Devin, et al., Tensorflow: Large-scale machine learning on heterogeneous distributed systems, arXiv preprint arXiv:1603.04467 (2016).

[50] S. L. Brunton, J. L. Proctor, J. N. Kutz, Discovering governing equations from data by sparse identification of nonlinear dynamical systems, Proceedings of the National Academy of Sciences 113 (2016) 3932–3937.